

Soft X-ray spectromicroscopy of nickel sorption in a natural river biofilm

A. P. HITCHCOCK,¹ J. J. DYNES,¹ J. R. LAWRENCE,² M. OBST,³ G. D. W. SWERHONE,³
D. R. KORBER⁴ AND G. G. LEPPARD¹

¹*Brockhouse Institute for Materials Research, McMaster University, Hamilton, ON, Canada*

²*National Water Research Institute, Saskatoon, SK, Canada*

³*Center for Applied Geoscience, Tuebingen University, Tuebingen, Germany*

⁴*Department of Food and Bioproduct Sciences, University of Saskatchewan, Saskatoon, SK, Canada*

ABSTRACT

Scanning transmission X-ray microscopy (STXM) at the C 1s, O 1s, Ni 2p, Ca 2p, Mn 2p, Fe 2p, Mg 1s, Al 1s and Si 1s edges was used to study Ni sorption in a complex natural river biofilm. The 10-week grown river biofilm was exposed to 10 mg L⁻¹ Ni²⁺ (as NiCl₂) for 24 h. The region of the biofilm examined was dominated by filamentous structures, which were interpreted as the discarded sheaths of filamentous bacteria, as well as a sparse distribution of rod-shaped bacteria. The region also contained discrete particles with spectra similar to those of muscovite, SiO₂ and CaCO₃. The Ni(II) ions were selectively adsorbed by the sheaths of the filamentous bacteria. The sheaths were observed to be metal rich with significant amounts of Ca, Fe and Mn, along with the Ni. In addition, the sheaths had a large silicate content but little organic material. The metal content of the rod-shaped bacterial cells was much lower. The Fe on the sheath was mainly in the Fe(III) oxidation state. Mn was found in II, III and IV oxidation states. The Ni was likely sorbed to Mn–Fe minerals on the sheath. These STXM results have probed nano-scale biogeochemistry associated with bacterial species in a complex, natural biofilm community. They have implications for selective Ni contamination of the food chain and for developing bioremediation strategies.

Received 08 May 2009; accepted 06 July 2009

Corresponding author: A. Hitchcock. Tel.: +1-905 525-9140 x24749; fax: +1-905 521-2773;
e-mail: aph@mcmaster.ca

INTRODUCTION

Micro-organisms abound in aqueous environments, where they are capable of sorbing and concentrating large quantities of metals, directly influencing the distribution, mobility and bioavailability of trace and contaminant metals alike. In nature, micro-organisms often congregate on surfaces to form biofilms, which are complex assemblies of multiple microbial species and extracellular polymeric substances (EPS), with multifarious architectures and biochemistry (Hall-Stoodley *et al.*, 2004; Branda *et al.*, 2005). Lalonde *et al.* (2007a), among others, have shown that metals are adsorbed by surface organic functional groups (e.g. carboxylic, amino) on microbial cells, on their extracellular structures (e.g. sheaths, S-layers) and by the EPS. The metal sorption capacity and surface chemistry vary considerably among and even within microbial species, which is attributed to differences in the surface organic groups, which in turn are responsive to

environmental parameters (e.g. pH, temperature, nutrients, electron acceptors) and the metal species (Neal *et al.*, 2007; Neu & Lawrence, 2008). Bioaccumulation of metals may result in the formation of authigenic minerals (e.g. biominerals) on the microbial surface (Toner *et al.*, 2005). These (bio)minerals formed on the microbial surfaces may also be capable of sorbing and concentrating metals from solution. Like the microbial species, there is considerable variation in the metal sorption capacity and properties among different authigenic minerals. Besides organic constituents and authigenic minerals, detrital materials trapped by the biofilm may also be sites for metal sorption (Lalonde *et al.*, 2007a). Determining the importance of each biofilm component (i.e. organic constituents, authigenic minerals and entrapped detrital material) in controlling metal sorption processes requires methods that are capable of obtaining chemical and speciation information about all of the biofilm components [microbial cells, EPS, (bio)-minerals, and detrital materials] at a relevant spatial

scale. Moreover, it is useful to carry out detailed assessments of natural, environmentally relevant samples (Lalonde *et al.*, 2007b) to evaluate whether processes observed in, or hypotheses based on pure culture studies (e.g. Yee & Fein, 2001) are consistent with these observations.

Soft X-ray scanning transmission X-ray microscopy (STXM) uses near-edge X-ray absorption fine structure (NEXAFS) spectroscopy as its contrast mechanism. It is capable of determining biochemical and metal speciation with a spatial resolution of better than 30 nm (Bluhm *et al.*, 2005). With suitable reference spectra, sequences of images recorded over a span of photon energies at core excitation edges can be converted to quantitative maps of specific chemicals in biological samples in hydrated environments. We have previously shown (Lawrence *et al.*, 2003; Dynes *et al.*, 2006b) that detailed analysis of image sequences at the C 1s edge may be used to provide quantitative maps of the major biomacromolecules (proteins, polysaccharides, lipids). In a separate study, the methodology for speciation and quantitative mapping of metals in complex biological systems via studies at the metal 2p edges was demonstrated and detection limits were evaluated (Dynes *et al.*, 2006a).

Nickel is a toxic metal found in aqueous environments as a result of various natural (e.g. acid rock drainage) and industrial (e.g. smelting) activities. Micro-organisms are known to bioaccumulate Ni (Rajendran *et al.*, 2002), and since micro-organisms are an important food source for other organisms (e.g. invertebrate grazers such as snails, mayflies, crustaceans), particularly in rivers (Lawrence *et al.*, 2002b, 2004), there is a concern that the food chain may be impacted in areas exposed to excess levels of Ni. Procedures for bioremediation of Ni-contaminated sites have been proposed (Salt *et al.*, 1998; Rajendran *et al.*, 2002). Investigations of the fate of Ni in natural aquatic environments can help understand how Ni is accumulated in the environment, which could give insight into food-chain effects and lead to improved bioremediation strategies. In a previous study (Dynes *et al.*, 2006a), a natural river biofilm was exposed to 1 mg L⁻¹ Ni²⁺ for 24 h, and examined with STXM at the O 1s and Fe, Mn and Ni 2p edges. That study demonstrated the methodology for quantitative metal mapping in complex biological systems and showed that, in the region examined, Ni was associated with Mn, and that Mn was associated with biology, possibly with a sheath of a filamentous algae or cyanobacteria. In this study, we examined a similar natural river biofilm exposed to 10 mg L⁻¹ Ni²⁺ for 24 h. The higher Ni concentration used in this study vs. the earlier study addressed a number of issues related to STXM sensitivity encountered at the lower Ni concentration. The 1 mg L⁻¹ Ni²⁺ was just above the detection limit using our acquisition conditions; a longer dwell time could have been used to increase the sensitivity but the risk of radiation damage would have increased. Also, at the lower Ni concentration, we would have been less certain that we were observing selective sorption of Ni by certain micro-organisms in the biofilm. Nevertheless, Ni concentrations of

10 mg L⁻¹ Ni²⁺ are typically found in watersheds contaminated from mine wastes (Ferris *et al.*, 1989a,b), thus the higher level was also of environmental relevance.

In natural biofilms there are often associated mineral phases containing Mn, Fe, Al, Si and Ca (Konhauser *et al.*, 1993, 1994; Lalonde *et al.*, 2007a,b; Peng *et al.*, 2007), which might interact with dissolved Ni. Thus, in addition to using STXM to quantitatively map the Ni, Fe and Mn species in the biofilm, Al, Si, Ca, K and Mg were also speciated and mapped. As we were interested in Ni sorption primarily on the biological entities in the biofilm, the C 1s edge was used to map carbonates and the major biomacromolecules, specifically protein, lipids and polysaccharides. The information from this multiple-edge STXM study was correlated and integrated to provide insight into Ni sorption mechanisms taking place in the biofilm.

MATERIALS AND METHODS

Sample preparation

The river biofilm was grown on the surface of removable polycarbonate slides in a rotating annular reactor at ambient temperature (20 °C), as described previously (Lawrence *et al.*, 2000, 2002a,b). Natural river water (South Saskatchewan River, Saskatoon, SK, Canada) collected in December 2004 and January 2005 was used as a source of nutrients and inoculum. Methanol (2 mg L⁻¹) was added to the water as a supplemental carbon source. The reservoir that fed the reactors was filled every 7 days throughout the 10-week development period. At the end of 10 weeks, the polycarbonate slide containing the biofilm was removed from the reactor and placed for 24 h in river water to which 10 mg L⁻¹ Ni²⁺ (as NiCl₂) had been added. After the 24 h Ni reaction period, the biofilm was aseptically scraped from the slide with a silicone spatula and placed in a sterile 1-mL microcentrifuge tube. An aliquot of the hydrated biofilm material was placed onto an X-ray translucent silicon nitride membrane (75 nm; Silson Ltd, Northampton, UK) and a second silicon nitride membrane was placed on top of the biofilm. The resultant silicon nitride sandwich (wet cell) was then sealed with acid-free silicone sealant to prevent drying and maintain the integrity of the biofilm. The sample was transported in a cooler via courier to the synchrotron and examined using X-ray microscopy within 7 days. The sample was stored at 4 °C when it was not being examined using X-ray microscopy.

The basic chemistry of the Saskatchewan River water was as follows: conductivity 45 mS m⁻¹, pH 8.5, turbidity 2.3 NTU, total Kjeldahl N 24 mg L⁻¹, and total hardness 185 mg L⁻¹ CaCO₃ (City of Saskatoon, Water Quality Department, personal communication). The typical concentrations of selected metals in the natural river water are listed in Table 1 (City of Saskatoon, Water Quality Department, personal communication). The chemical equilibria of the

Table 1 Concentration of selected metals in the South Saskatchewan River water at Saskatoon, SK, Canada

Metal	Concentration ($\mu\text{g L}^{-1}$)
Mn	10–20
Ni	1–2 [*]
Si	40–60
Al	5–20
Mg	16 000–18 000
Ca	43 000–47 000
K	2800–3400
Fe	20–60

*The 10-week old biofilm was exposed to $10\,000\ \mu\text{g L}^{-1}$ Ni as NiCl_2 for 24 h. Source: City of Saskatoon, Water Quality Department, personal communication.

Saskatchewan River water were modeled using PHREEQC Interactive (version 2.8; Wateq4f database; Parkhurst & Appelo, 1999). PHREEQC is based on an ion-association aqueous model and has capabilities for calculating the speciation and saturation-index under various geochemical conditions. Values of $\text{pH} = 8.5$, $P = 0.04\ \text{mg L}^{-1}$, $N = 0.7\ \text{mg L}^{-1}$, $\text{pe} = 4$, and $\log P(\text{CO}_{2(\text{g})}) = -3.414$ and the concentrations listed in Table 1 were used to calculate the speciation expected for these elemental concentrations.

Scanning transmission X-ray microscopy

X-ray imaging and spectromicroscopy were carried out at the Advanced Light Source (ALS, Berkeley, CA, USA) using STXM microscopes (Kilcoyne *et al.*, 2003) at beamlines 5.3.2 (Warwick *et al.*, 2002) and 11.0.2 (Warwick *et al.*, 2004). The Mn 2p, Fe 2p, Ni 2p, Mg 1s, Al 1s, Si 1s and O 1s absorption edge studies were performed on STXM beamline 11.0.2. The C 1s, K 2p and Ca 2p absorption edge studies were performed on STXM beamline 5.3.2. The measured transmitted signals (I) were converted to optical densities [absorbance, $\text{OD} = -\ln(I/I_0^{-1})$] using incident flux (I_0) measured through regions of the wet cell devoid of biofilm, to correct for the absorbance by the silicon nitride membranes and the water in the wet cell. For the data in this study, the biofilm sample was fully wet during the first set of measurements (February, 2005), but was only partially hydrated at the time of the final STXM measurements (November, 2005). The O 1s, Fe 2p, Mn 2p, Ni 2p, K 2p, Ca 2p and C 1s data were collected (in that order) in February 2005 (some repeated in November 2005), while the Si, Mg and Al 1s data were collected in November 2005. The details of the Fe 2p, Mn 2p and Ni 2p metal edge spectra extracted from the biofilm in the study area at the two time periods were the same, indicating that the change in the hydration state of the biofilm did not affect the metal speciation. However, upon drying, there was some deformation of some regions of the biofilm but not in the area of the sheaths.

Radiation damage is a significant concern in X-ray microscopy, especially in this work as we have examined

exactly the same area at many different core edges. This was an intentional strategy as we wished to use comparisons of the speciation and spatial distribution of the different metals as a major tool in understanding Ni sorption in the biofilm. To minimize possible effects on our results, we measured those edges where radiation damage is known to modify oxidation state speciation – Fe 2p and Mn 2p (Toner *et al.*, 2005) – before measuring the Ni 2p or C 1s edges. To gain confidence that the integrated dose was not causing significant changes to the speciation, we regularly measured images over an area larger than the main stack area. This is a useful routine strategy as the microscope operates in a line-at-a-time mode whereby the beam is sitting $\sim 1\ \mu\text{m}$ to the left of the start position of each horizontal scan line for about 10 times longer than in any pixel in the stack. If the material suffers radiation damage, these start areas (and to a lesser extent, a deceleration region at the right side of the stack area) become clearly visible as a vertical line outside the imaged area, especially when measured at 289 eV [the $\sigma^*(\text{C}-\text{O})$ peak of polysaccharides]. The Supporting Information (Fig. S1) contains a comparison of these expanded area images taken throughout the whole measurement period, and in addition shows an example of the damage visualization in a case from a different sample where damage has occurred. We do not claim that the measurements reported herein were carried out without causing some radiation damage to the sample. However, compared with many other STXM measurements we have made, these are well within the grouping of studies we consider to have experienced ‘minimal radiation damage’. It is possible that some of the metal speciation results are skewed towards a more reduced state due to radiation reduction, but we think this is a minor effect, and that issues with regard to availability of suitable reference spectral standards place greater limitations on our results than radiation damage.

The absolute energy scale in the Fe 2p region was set by assigning the energy of the second peak in the Fe $2\text{p}_{3/2}$ signal of $\text{FeCl}_3 \cdot 6\text{H}_2\text{O}$ to 709.8 eV (Dynes *et al.*, 2006a), the value found when the spectrometer had been recently calibrated using N_2 , O_2 , Ne and Al_2O_3 . We estimate the accuracy of this calibration to be ± 0.2 eV. Similarly, for NiO and $\text{MnSO}_4 \cdot 7\text{H}_2\text{O}$, the primary peaks in the $2\text{p}_{3/2}$ signals were set to 853.2 eV (van der Laan *et al.*, 1986) and 639.8 eV (Chen & Sette, 1990) respectively; for O 1s, the peak of the π^* signal of protein was set to 532.1 eV (Stewart-Ornstein *et al.*, 2007); for Al 1s, the $1\text{s} \rightarrow 4\text{p}$ peak of muscovite was set to 1570.4 eV (Yoon *et al.*, 2004); for Si 1s, the t_2 peak of SiO_2 was set to 1846.8 eV (Li *et al.*, 1994); for Ca 2p, the main $2\text{p}_{1/2} \rightarrow 3\text{d}$ peak in CaCO_3 was set to 352.6 eV (Benzerara *et al.*, 2004).

Data analysis

The methodology used to quantitatively map the major biomacromolecules and metal species in the biofilm has been described in detail elsewhere (Dynes *et al.*, 2006a,b). Briefly,

the total concentration of a given species was mapped in one of two ways: (i) the difference between two images, one measured at the energy of a strong characteristic absorption feature and the other measured at an energy below the onset of absorption for that species. The image difference map was made quantitative by converting the change in the optical density (ΔOD) scale to effective thickness (in nm) using a scaling factor determined from the linear absorbance (optical density per nm) for a specific compound at the two photon energies. (ii) The difference in the sum of images in the core level continuum and those before the onset of the core edge structure, taken from the image sequence. The first method gave more detailed maps since a greater pixel density was used. However, in cases where there was multiple oxidation states (Mn 2p), we preferred to use the continuum signal as this would not be affected by spatial variation in the oxidation states. For majority species, there is an estimated 20% uncertainty in the quantification that is associated with possible systematic errors in the conversion from optical density to effective thickness, as discussed in detail elsewhere (Dynes *et al.*, 2006a). These values reflect our limited knowledge of the actual composition and thus inability to provide an accurate set of reference spectra. The energies and scaling factors used for the quantification of the image difference maps (on-resonance minus off-resonance) for each element are listed in Table 2.

The metal and biochemical speciation were derived from the analysis of image sequences, a series of images (typically 60–100) collected at each absorption edge. The mapping process involves fitting a linear combination of quantitative reference spectra (see below) and the calculated spectrum of H_2O , which has no spectral features at the edges examined (Dynes *et al.*, 2006a), to the measured spectrum at each pixel. Subsequent spectral checks (e.g. examination in the energy domain, optimum number of components, amplitude of the residual remaining after the fit; Dynes *et al.*, 2006a,b) lead to an iterative improvement of the selection of reference spectra used to explain the data at each edge. The component maps were

Table 2 Energies, scaling factor and reference compounds used to map the total concentration of each element using image difference maps

Edge	Pre-edge (eV)	Peak (eV)	Scale factor (nm^{-1})	Reference compound
C 1s	282.0	288.2	0.0091	Albumin
O 1s	529.0	532.1	0.0096	Albumin
Mn 2p	637.0	639.7	0.035	Rhodochrosite ($MnCO_3$)
Ni 2p	848.0	850.0	0.008	NiO
Si 1s	1830.0	1846.8	0.0015	$CSi_2O_{10}H_{10}^*$
Al 1s	1555.0	1570.4	0.002	Muscovite ($KAl_2(AlSi_3O_{10})(OH)_2$)
Mg 1s	1303.0	1314.0	na [†]	na
Ca 2p	350.2	352.6	0.015	Aragonite ($CaCO_3$)
Fe 2p	704.0	709.8	0.015	$FeCl_3 \cdot 6H_2O$

*See text for details.

†Not applicable.

obtained by singular value decomposition (SVD) (Dynes *et al.*, 2006a). Image and spectral processing was performed with aXis2000 (Hitchcock, 2008).

The elemental composition of the filamentous sheaths was determined by fitting the measured optical density edge jumps to scaled mass absorption coefficients (Henke *et al.*, 1993). This approach desensitizes the analysis to the exact species that may be present, which is a concern with regard to the spectral fitting procedure used to generate the speciation maps. However, there are uncertainties associated with differences in density among the chemical species present in a given area of interest, so one must be cautious in interpreting these results in terms of an atomic composition.

Reference spectra

Reference spectra of well-known, homogeneous model compounds were used to identify and quantify the unknown species in the samples. The reference spectra were placed on an absolute linear absorbance scale by matching them to the predicted response for the compound based on its elemental composition and density, using tabulated continuum absorption coefficients (Henke *et al.*, 1993). Using these quantitative reference spectra yielded quantitative effective thickness scales (in nm) from the fitting analysis or from the image difference mapping. The precision of the SVD fitting procedure has been estimated previously to be in the range of a few per cent (Dynes *et al.*, 2006b). The accuracy is more limited because of systematic errors such as incorrect linear absorbance scales of the reference spectra and incorrect selection of model compounds for fits.

Quantitative reference spectra of $FeCl_3 \cdot 6H_2O$ [Fe(III)], $FeCl_2 \cdot 4H_2O$ [Fe(II)], NiO [Ni(II)], human serum albumin (protein), 1,2-dipalmitoyl-sn-glycero-3-phosphocholine (lipid), xanthan gum (polysaccharide) and K^+ (K_2CO_3 with the signal of $CaCO_3$ subtracted to remove the C 1s spectrum of the carbonate anion) were determined previously (Dynes *et al.*, 2006a,b). The Al 1s and Si 1s reference spectra of muscovite were determined for this study using a muscovite sample from the Stanford Mineral Collection. A density of 2.82 g cm^{-3} and a structural formula of $KAl_2(AlSi_3O_{10})(OH)_2$ were used. Other Si 1s reference spectra used in the fitting included: coesite (SiO_2) ($d = 3 \text{ g cm}^{-3}$; Li *et al.*, 1994), an organo-silicon compound ($(CH_3)_3Si-OCH_3$) ($d = 2 \text{ g cm}^{-3}$; Urquhart *et al.*, 1997) and an internal reference spectrum for an 'organosilicate' species that dominated the sheath region, derived as described below in the Results section. The Mn 2p reference spectra were digitized from the literature (Waychunas, personal communication) and included rhodochrosite ($MnCO_3$) [Mn(II)] ($d = 3.69 \text{ g cm}^{-3}$), reagent grade $MnOOH$ [Mn(III)] ($d = 4.34 \text{ g cm}^{-3}$) and ramsdellite (MnO_2) [Mn(IV)] ($d = 4.37 \text{ g cm}^{-3}$). In all cases, the reference spectra were made quantitative using the tabulated continuum absorption coefficients (Henke *et al.*, 1993) and indicated densities.

RESULTS

Biofilms in natural environments develop heterogeneous microbial communities with complex architectures and chemistries at the nano- and micro-scale, and STXM allows one to access the chemical conditions present at these spatial scales. Large area survey image difference maps provide a means to rapidly locate areas of interest, ones containing specific metals along with microbial communities. Figure 1A presents an overlay of the Ni 2p image difference map ($I_{852.7}-I_{850}$) on the O 1s image difference map ($I_{532}-I_{529}$) for a $140 \times 80 \mu\text{m}$ area of the river biofilm. The 532-eV signal is dominated by O 1s $\rightarrow \pi^*_{\text{C=O}}$ transitions in protein and readily reveals the microbes. Even at this relatively low spatial resolution, the individual microbial cells/cellular components, the extracellular polymeric structures (EPS) and areas with significant Ni (bio)-accumulation are clearly evident. From this larger region, we selected a $16 \times 20 \mu\text{m}$ subregion (white dotted rectangle, Fig. 1A) for a detailed study. This area was rich in both Ni and biology, allowing study of the dependence of Ni

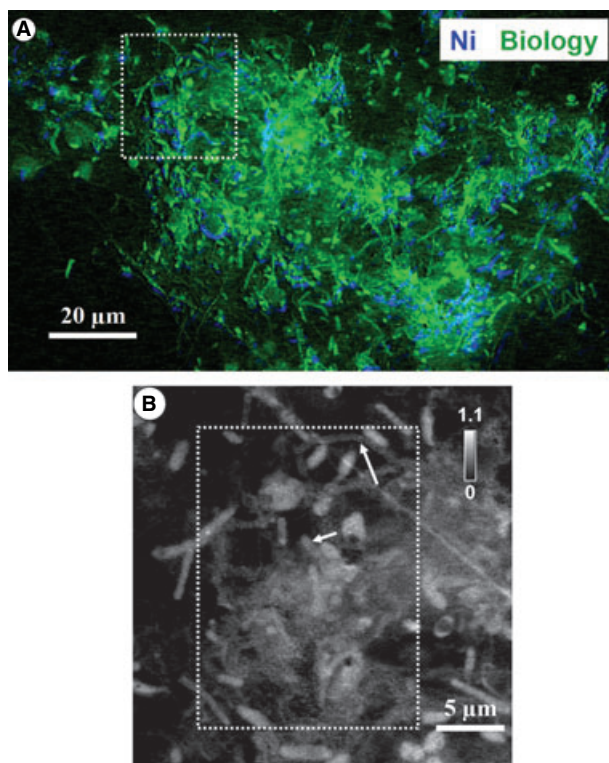


Fig. 1 Scanning transmission X-ray microscopy optical density (OD) images of the wet river biofilm. (A) Overview-overlay of Ni map ($OD_{852.7}-OD_{850}$) (blue) on the biology map ($OD_{532.1}-OD_{529}$) (green) over a large region ($140 \mu\text{m} \times 80 \mu\text{m}$). (B) Protein map ($OD_{288.2}-OD_{282}$) in a $30 \mu\text{m} \times 30 \mu\text{m}$ subarea defined by the dotted rectangle in Figure 1A. The white dotted rectangle in Figure 1B shows the area where the metal speciation and biochemistry were studied in detail. The gray scales indicate OD. The short and long arrows indicate typical examples of rod-shaped bacteria and the sheaths of filamentous bacteria respectively.

sorption on microbial morphotypes, biochemistry and the presence of other metal species. The C 1s image difference map ($I_{288.2}-I_{280}$) of this subregion is presented in Fig. 1B. The signal at 288.2 eV is dominated by the strong C 1s $\rightarrow \pi^*_{\text{C=O}}$ band of the amide carbonyl of protein (Stewart-Ornstein *et al.*, 2007), although there are also spectral contributions at this energy from lipids and polysaccharides (Lawrence *et al.*, 2003; Brandes *et al.*, 2004). With the higher spatial sampling, individual microbial cells/cellular components and the EPS are now clearly distinguishable. Both sheaths of filamentous bacteria and rod-shaped bacterial cells are visible. Typical examples of each are indicated by short and long arrows respectively in Fig. 1B.

Mapping biochemistry

The C 1s X-ray absorption spectra of the major biomacromolecules (i.e. protein, lipids, polysaccharides) and carbonates have characteristic features that allow them to be differentiated and mapped in a biofilm (Lawrence *et al.*, 2003; Dynes *et al.*, 2006b). Spectral fitting of the C 1s image sequence with protein, lipid, polysaccharide, carbonate and K was conducted, giving rise to the component maps presented in Fig. 2A–E. Note that the K 2p and C 1s signals overlap and thus both can be measured in the same image sequence. The K results are discussed in a later section. Spectra derived from the protein, lipid, polysaccharide and carbonate component maps, based on threshold masking of the regions with high-intensity pixels (regions not shown), are plotted in Fig. 3, allowing comparison with the reference spectra. The match to the reference spectra is not perfect, in part, because the selected regions contain a mixture of the biomacromolecules and carbonate. Nevertheless, it is clear that this region of the biofilm contains proteins, lipids, polysaccharides and carbonates. Figure 2F presents a color-coded composite map of the lipid, protein and carbonates. The major biomacromolecules mapped in the rod-shaped bacteria were protein and lipids, whereas only lipids were detected in the sheaths of the filamentous bacteria. The sheaths of the filamentous bacteria only contained a little carbonate ($5 \pm 3 \text{ nm}$) but there was no detectable carbonate signal associated with the rod-shaped bacteria. Discrete particles of carbonate were also present in this region of the biofilm with an average thickness of $50 \pm 20 \text{ nm}$. Extracellular polymeric structures were apparent in the biofilm from the polysaccharide map; however, they were not found in association with the rod-shaped bacteria or the sheaths of the filamentous bacteria (i.e. it was unbound EPS).

Metal speciation and mapping

Nickel

Figure 4A displays the Ni image difference map showing the distribution of Ni in this region of the biofilm. Comparing the

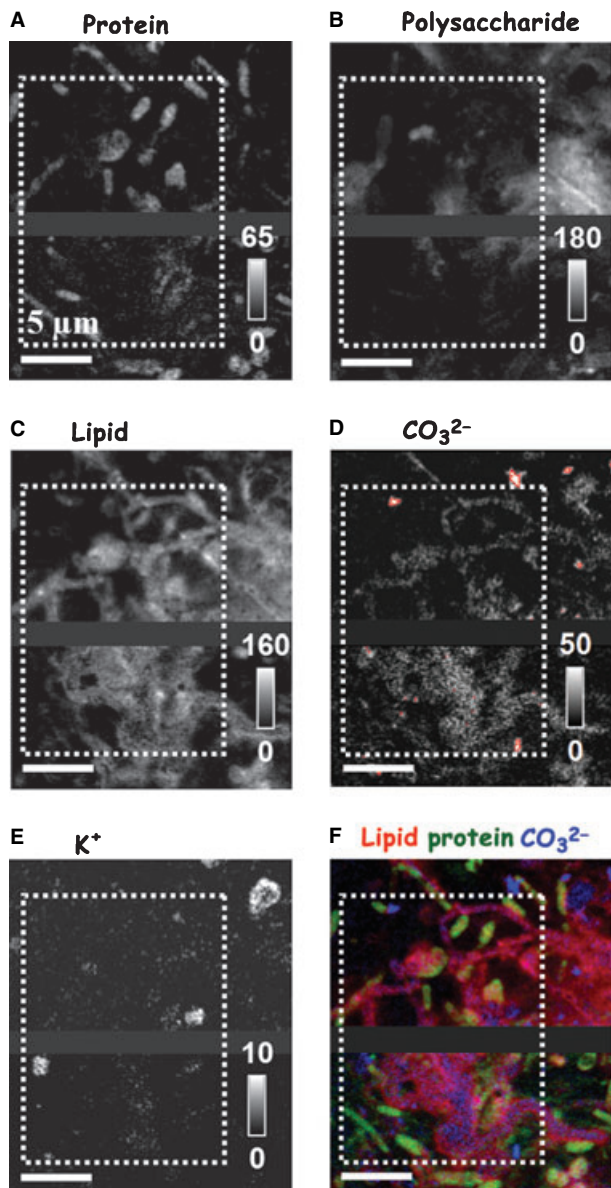


Fig. 2 C 1s and K 2p results. Component maps (A) protein, (B) polysaccharides, (C) lipids, (D) carbonates (red = 50–140 nm effective thickness) and (E) K. The component maps were derived by spectral fitting of the image sequence (84 OD images between 280 and 310 eV) using the spectra of the reference compounds (Fig. 3), and (F) color-coded composite map of lipid, protein and carbonates (red = lipid, green = protein, blue = carbonate). The gray scales indicate thickness in nanometers. The band in the middle of each map is a region of missing data that was not sampled, as the C 1s data was recorded in two sections.

Ni map to the biology map (Fig. 1B) indicates that essentially all of the Ni was located on the sheaths of the filamentous bacteria, with a distinctly enhanced level of Ni at the edges of the filamentous sheaths. Ni(II) compounds are easily distinguishable from Ni metal as the main Ni 2p_{3/2} peak occurs about 2 eV higher and is much more prominent for the Ni(II)

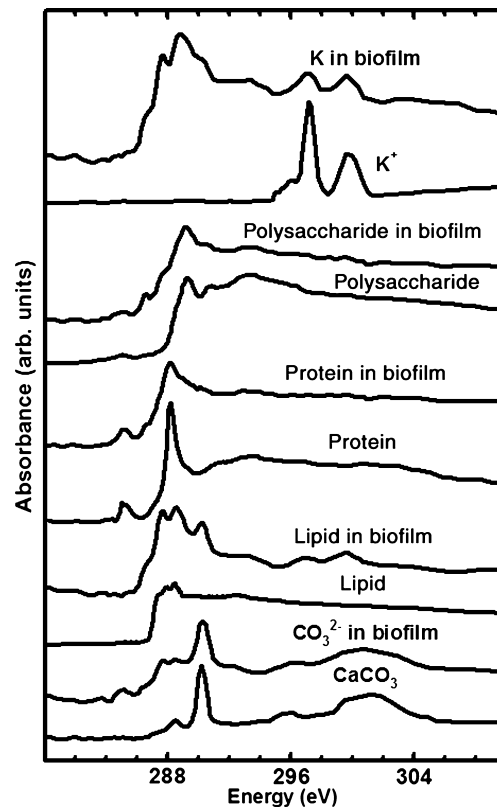


Fig. 3 C 1s and K 2p X-ray absorption spectra of the reference compounds aragonite (CaCO₃), protein (human serum albumin), lipid (1,2-dipalmitoyl-sn-glycero-3-phosphocholine), polysaccharide (xanthan gum) and K⁺ (K₂CO₃ with the signal of CaCO₃ subtracted to remove the C 1s spectrum of the carbonate anion) compared with spectra derived by threshold masking of high-intensity pixels in the respective component map (Fig. 2).

compounds (Krasnikov *et al.*, 2007). It is clear that the Ni in the biofilm is in the II oxidation state, which is not unexpected as it was added as Ni(II). The Ni 2p absorption spectra of different Ni(II) compounds have only subtle differences in spectral lineshape (van der Laan *et al.*, 1985, 1986; van Elp *et al.*, 1994), which precluded us from identifying more than one Ni(II) species in the biofilm. The Ni 2p image sequence was fit using the spectrum of NiO as a reference. The spectrum derived from the Ni(II) component map, based on threshold masking of the regions with high-intensity pixels (region not shown) is plotted in Fig. 4B, in comparison with the spectrum of NiO. The Ni(II) component map derived by spectral fitting (not shown) was similar to that of the image difference map (Fig. 4A).

Manganese

The total distribution of Mn in this region of the biofilm, determined from the difference of a set of 10 post-edge images and 14 pre-edge images in the Mn 2p image sequence, is shown in Fig. 5A. Comparison with the biology map (Fig. 1B) showed that the Mn was mostly located on the

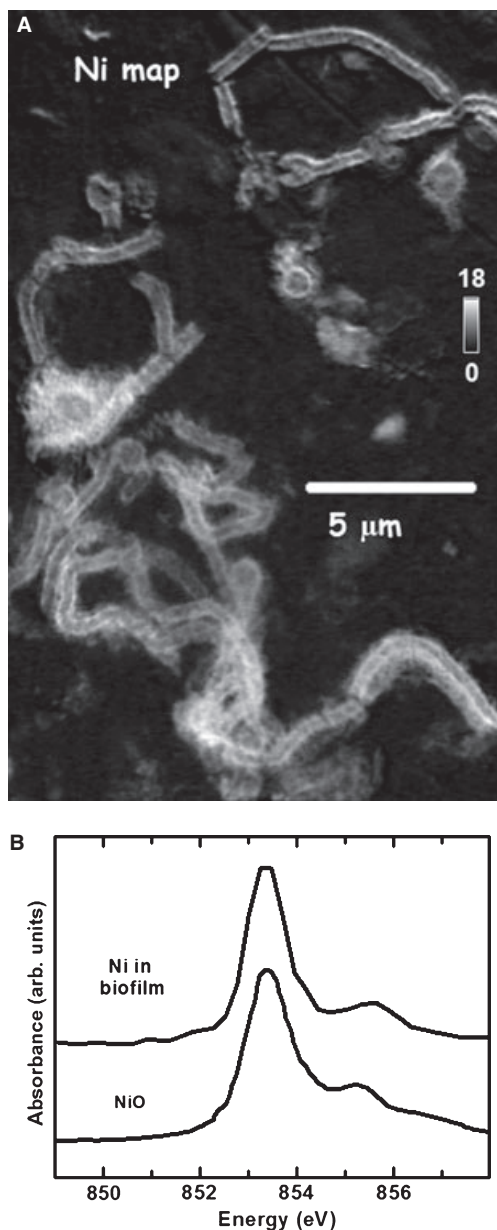


Fig. 4 Ni 2p results. (A) Ni image difference map ($OD_{852.7} - OD_{850}$). The gray scale indicates effective thickness in nanometers. (B) Ni 2p X-ray absorption spectrum of NiO compared with the spectrum derived by threshold masking of high-intensity pixels in the Ni(II) component map determined by spectral fitting of the Ni 2p image sequence (36 OD images between 846 and 858 eV) using the NiO spectrum.

filamentous bacterial sheaths and that there were localized hot spots of Mn at the edges of the filamentous sheaths. The details of the Mn 2p absorption spectrum depend strongly on the Mn oxidation state (Toner *et al.*, 2005), as shown for the reference compounds $MnCO_3$ [Mn(II)], $MnOOH$ [Mn(III)] and MnO_2 [Mn(IV)] (Waychunas, personal communication) plotted in Fig. 5B. In some cases, the site symmetry and ligands can be identified from the differences in spectral

lineshape (Grush *et al.*, 1996). The Mn 2p image sequence was fit using the spectra of $MnCO_3$, $MnOOH$ and MnO_2 . Spectra derived from the Mn(II), Mn(III) and Mn(IV) component maps (Fig. 5C–E), based on threshold masking of the regions with high-intensity pixels (regions not shown), are plotted in Fig. 5B, in comparison with the reference spectra. It is clear that this region of the biofilm contained Mn in each of these three oxidation states. However, it was not possible to identify particular Mn species, in part because each of the selected regions contained a mixture of Mn(II), Mn(III) and Mn(IV) species, and in part due to the possibility of mixed-oxidation-state Mn species. The relative amounts of Mn(II), Mn(III) and Mn(IV) in this region of the biofilm were 40%, 20% and 40% respectively, determined by summing the signal for each Mn species from the component maps. We note that we did not make spectroscopic checks for radiation damage at the Mn edge by repeating the measurement. Toner *et al.* (2005) examined radiation damage by repetitive measurements of the Mn 2p spectrum of acid birnessite (Mn(IV) oxide) suspended in organic medium, and determined that there was relatively minor changes in the shape of the Mn 2p spectrum but a measurable loss of the total Mn(IV) signal, amounting to 5% reduction after the first of three successive stacks. In this multi-edge study, very short dwell times were used ($0.4\text{--}0.6\text{ ms pixel}^{-1}$) and the Mn edge was the third image sequence measured. The Supporting Information (Fig. S1) shows images of the studied region acquired throughout the whole sequence of measurements. There is very little evidence of radiation damage as judged by changes in morphology, a criteria also used by Toner *et al.* (2005) in monitoring damage in their study. Although we are reasonably confident that radiation damage plays a minimal role in our study, it is possible that the amount of Mn(III) and Mn(IV) may be underestimated on account of some reduction. The issue of possible radiation damage affecting the Mn speciation is discussed in greater detail in the Supporting Information, which shows results of an analysis in which the Mn 2p signal is isolated from the total signal by subtracting the non-Mn signal. Figure 5F presents a color-coded composite map of the three Mn oxidation state species. The Mn species are spatially heterogeneous. In general, there is a greater amount of the higher oxidation states of Mn at the exterior of the sheaths, and greater amounts of the lower oxidation states towards the interior of the sheaths, although there are some sheath areas with predominantly Mn(II) (top right), and others with predominantly Mn(IV).

Iron

Figure 6A presents the Fe image difference map showing the distribution of Fe in this region of the biofilm. Note that regions with more than 10 nm of Fe per pixel are indicated in red. The sheaths of the filamentous bacteria were encrusted with Fe. The rod-shaped bacteria did not bioaccumulate Fe. There were also some discrete particles containing Fe in the

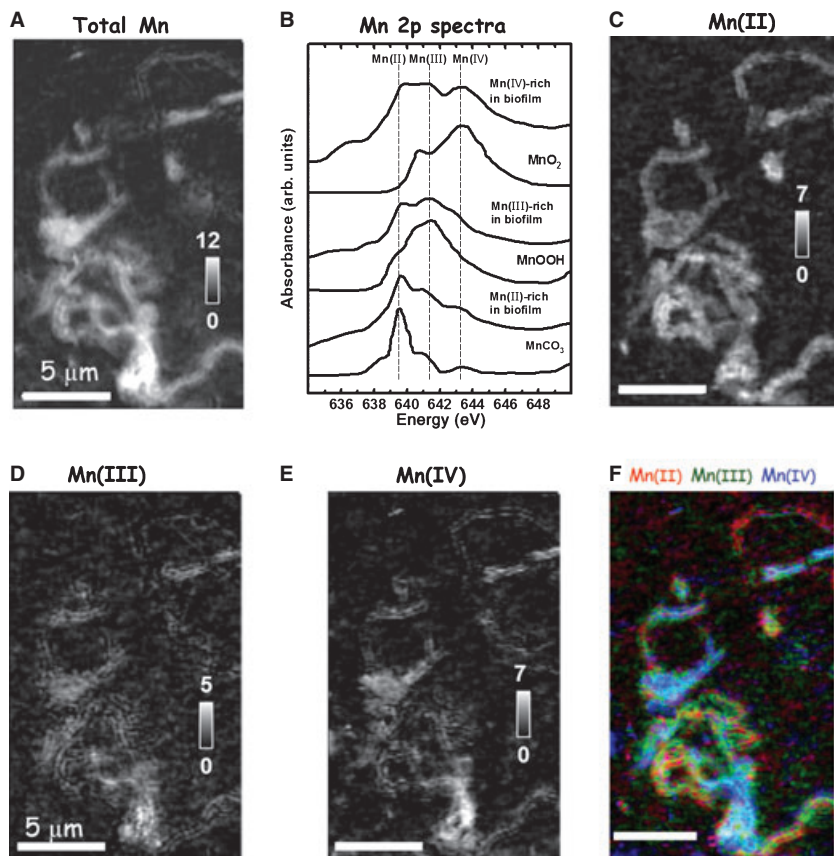


Fig. 5 Mn 2p results. (A) Total Mn map determined from the difference of the sum of 14 images from 634 to 638 eV (pre-Mn 2p) and the sum of 10 images from 645 to 650 eV (Mn 2p continuum). (B) Mn 2p X-ray absorption spectra of reference compounds rhodochrosite (MnCO_3), MnOOH reagent and ramsdellite (MnO_2) (Waychunas, personal communication), compared with spectra derived by threshold masking of the high-intensity pixels in the Mn(II), Mn(III) and Mn(IV) component maps (C–E). (C) Mn(II) component map, (D) Mn(III) component map and (E) Mn(IV) component map. The component maps were derived by fitting the image sequence (58 OD images between 634 and 650 eV) to the spectra of the Mn(II), Mn(III) and Mn(IV) reference compounds and a spectrum extracted from the image sequence from regions without detectable Mn. (F) Color-coded composite map of the Mn(II) (red), Mn(III) (green) and Mn(IV) (blue) component maps. The gray scales indicate thickness in nanometers.

biofilm that were not in association with the bacterial sheaths or rod-shaped bacteria.

The Fe oxidation state was determined from the shape of the Fe $2p_{3/2}$ signal that has two main peaks, with the peak at 708 eV being the strongest for Fe(II) species and that at 709.8 eV the strongest for Fe(III) species (Dynes *et al.*, 2006a), as seen in the $\text{FeCl}_3 \cdot 6\text{H}_2\text{O}$ and $\text{FeCl}_2 \cdot 4\text{H}_2\text{O}$ reference spectra (Fig. 6B). Although it is frequently assumed that the intensity of the 708-eV peak can be used as a measure of Fe(II) content and the intensity of the 710-eV peak as a measure of the Fe(III) content, this is incorrect as the relative intensities of these two peaks depend on other factors such as local geometry and the nature of the ligands, in addition to the oxidation state. This assumption is particularly suspect for Fe-containing minerals with mixed oxidation states [Fe(II,III)] (Peng *et al.*, 1995; Supporting Information of Dynes *et al.*, 2006a). Rather than making this questionable assumption, we have chosen to fit the Fe 2p image sequence

using two iron chloride reference spectra to obtain Fe(II) and Fe(III) component maps (Fig. 6C,D). We note that, although this choice is improvement over the simple assumption of correlating the 708- and 710-eV peaks with Fe(II) and Fe(III), the accuracy of the answer obtained will depend on how similar the spectra of the Fe(II) and Fe(III) species present in the sample are to the spectra of the iron chloride species. Spectra from Fe(II)-rich and Fe(III)-rich regions were derived by threshold masking regions with high-intensity pixels in the maps (regions not shown). These spectra are plotted in Fig. 6B, in comparison with the reference spectra. This spectral comparison suggests there were at least two distinct Fe species in this region of the biofilm. This conclusion is based on changes in different regions of the relative intensities of the double peaks at the Fe $2p_{3/2}$ -edge (708 and 710 eV) and a slight difference in lineshape. The 710-eV peak was the most intense in both types of spectra, indicating that both Fe species contained Fe(III). However, the spectrum where the

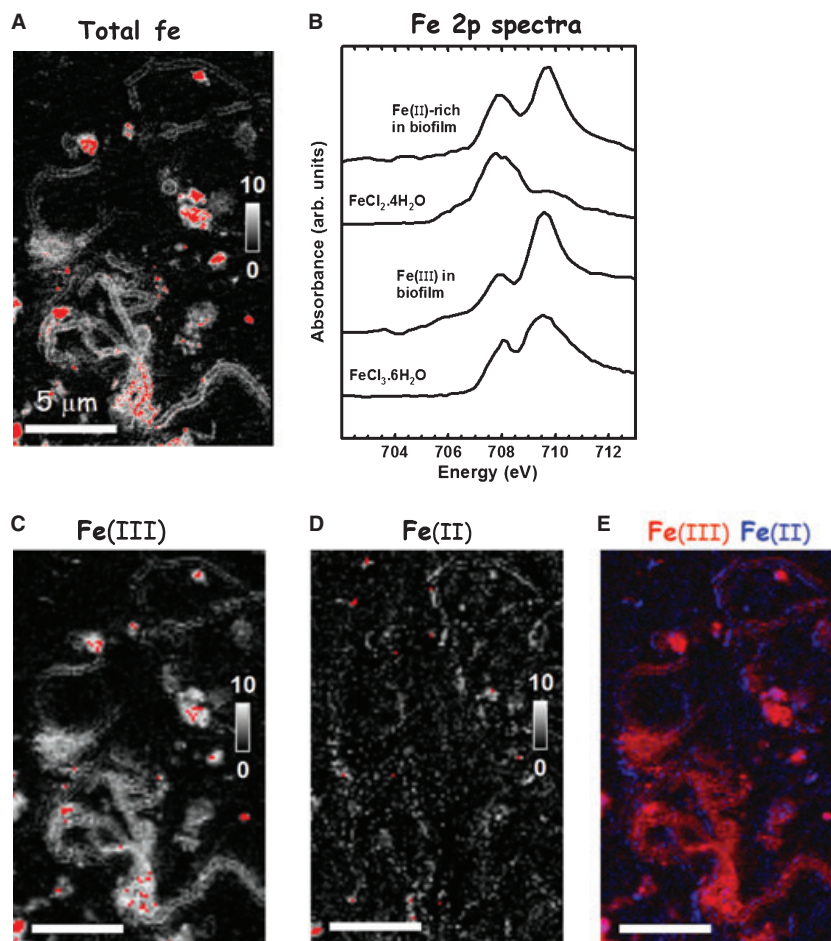


Fig. 6 Fe 2p results. (A) Fe image difference map ($OD_{709.8} - OD_{704}$). The red areas represent areas with Fe effective thickness between 10 and 40 nm. (B) Fe 2p X-ray absorption spectra of reference compounds $FeCl_3 \cdot 6H_2O$ and $FeCl_2 \cdot 4H_2O$ compared with spectra derived by threshold masking of the high-intensity pixels in the Fe(II) and Fe(III) component maps (C–D). (C) Fe(III) component map (red areas represent areas with Fe effective thickness between 10 and 40 nm) and (D) Fe(II) component map (red areas represent areas with Fe effective thickness between 10 and 15 nm). The component maps were derived by spectral fitting of the image sequence (53 OD images between 698 and 713 eV) using the spectra of the reference compounds. (E) Color-coded composite map (individually rescaled) of the Fe(III) and Fe(II) species component maps [red = Fe(III), blue = Fe(II)]. The contrast in the composite map has been adjusted to better visualize the Fe(III) component in the biofilm, particularly in the region of the filamentous sheath. The gray scales indicate thickness in nanometers.

708- and 710-eV intensities were more similar, and had a broader 708-eV peak, was interpreted to mean that these regions also contained some Fe(II) species. It is possible that some of the Fe(II) signal could have originated from beam damage. However, based on our previous study (Dynes *et al.*, 2006a), radiation damage was not evident at the Fe 2p-edge after a similar irradiation period of a similar biofilm. It was not possible to identify either Fe species as a specific compound but rather to map the amounts of the Fe(III)-rich and (relatively) Fe(II)-rich species. The amounts of Fe(III)-rich and Fe(II)-rich species in the study area were 70% and 30% respectively, determined by summing the effective thickness per pixel for each Fe species from the component maps. Figure 6E displays the color-coded composite map of the two Fe-oxidation states species. The sheaths of the filamentous bacteria bioaccumulated mainly the Fe(III)-rich species, and only a

small amount of the Fe(II)-rich species. In contrast, some of the discrete particles contained mainly Fe(III), while other particles appeared to be predominantly composed of Fe(II).

Calcium

Ca 2p absorption spectra exhibit a complex fine structure, which is well suited to differentiate $CaCO_3$ polymorphs and Ca phosphates (Himpfel *et al.*, 1991; Nafel *et al.*, 2001; Benzerara *et al.*, 2004). There is a strong Ca 2p $2p_{1/2} \rightarrow 3d$ peak at 352.6 eV in all species and this was used for Ca quantitation. The distribution of Ca in this region of the biofilm is displayed in the Ca image difference map (Fig. 7). Ca 2p signal was found on the sheaths of the filamentous bacteria but not on the rod-shaped bacterial cells. There were also discrete particles containing Ca, which, when compared with the carbonate map (Fig. 2D), can be identified as $CaCO_3$. The C 1s

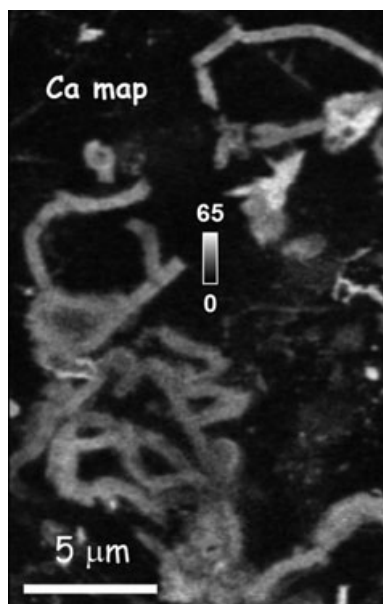


Fig. 7 Ca 2p results. Ca image difference map ($OD_{352.6} - OD_{350.3}$). The gray scale indicates thickness in nanometers.

spectrum of the sheath (see the separate section on the sheath below) showed the characteristic sharp peak at 290.3 eV, from C 1s $\rightarrow \pi^*_{C=O}$ transitions only very weakly, such that most of the Ca in the filamentous sheaths must be from some other mineral, perhaps a calcium silicate or calcium phosphate.

Silicon

The distribution of Si in the biofilm is shown in Fig. 8A. This was determined from the difference in sums of 10 pre-edge images, and 20 images in the Si 1s continuum (1852–1862 eV), taken from the Si 1s image sequence. Comparison with the biology map (Fig. 1B) shows that Si was found on the sheaths of the filamentous bacteria but not on the rod-shaped bacterial cells. There were also discrete particles that contained Si, some, but not all of which matched the discrete particles that were found to be high in Al (see next section).

The Si 1s-edge absorption spectra of Si compounds have different shapes and the position of the absorption maximum is dependent primarily not only on the oxidation state [the net Si(0)–Si(IV) shift is ~ 8 eV], but also on the coordination number, polymerization of SiO_4^{4-} , Si–O bond distance, Si–O bond valence, distortion of SiO_4^4 tetrahedra, and chemical substitution in both tetrahedral and octahedral sites (Li *et al.*, 1993, 1994, 1995; Urquhart *et al.*, 1997). The Si 1s spectra of silicate minerals have their strongest peak centered at 1846.4 ± 0.3 eV (Li *et al.*, 1995), the polymorphs of SiO_2 (e.g. coesite, α -quartz) have a maximum centered at 1846.7 ± 0.3 eV (Li *et al.*, 1994), while organosilicon compounds have their maximum centered considerably lower, between 1844 and 1845 eV (Urquhart *et al.*, 1997).

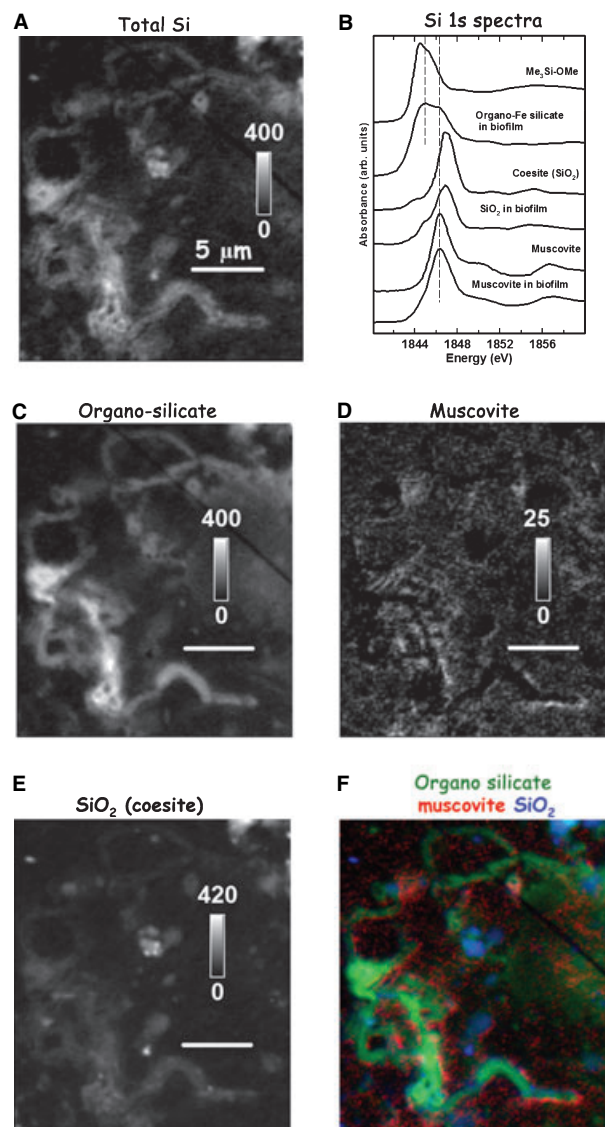


Fig. 8 Si 1s results. (A) Total Si map determined from the difference of the sum of images from 1839 to 1844 eV (pre-Si 1s) and the sum of images from 1852 to 1862 eV (Si 1s continuum). (B) Si 1s X-ray absorption spectra of reference compounds muscovite and coesite (Li *et al.*, 1994) and $(CH_3)_3Si-OCH_3$ (Urquhart *et al.*, 1997), compared with spectra derived by threshold masking of the high-intensity pixels in the muscovite, organo-silicate and SiO_2 component maps. (C) organo-silicate component map; (D) muscovite component map and (E) SiO_2 (coesite) component map. The component maps were derived by spectral fitting of the image sequence (70 images between 1835 and 1860 eV) to the spectra of coesite, muscovite and an internal organo-silicate spectrum. (F) Rescaled color-coded composite map of the muscovite, SiO_2 and organo-silicate component maps (red = muscovite, green = organo-silicate, blue = SiO_2). The gray scales indicate thickness in nanometers.

The Si 1s image sequence was fit to muscovite (silicate mineral), coesite (SiO_2) and $(CH_3)_3Si-OCH_3$ (organosilicon) using the reference spectra plotted in Fig. 8B. The derived organo-silicate, muscovite and coesite maps are shown in Fig. 8C–E respectively. There are discrete

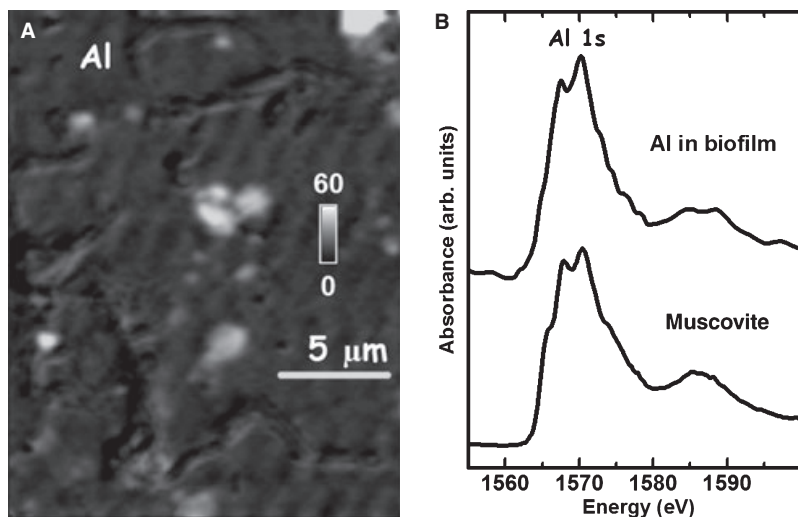


Fig. 9 Al 1s results. (A) Al distribution determined from the difference of the sum of images from 1555 to 1562 eV (pre-Al 1s) and the sum of images from 1565 to 1575 eV (Al 1s continuum). Note that the diagonal streaking pattern is an artifact. The gray scale indicates thickness in nanometers. (B) Al 1s X-ray absorption spectrum of muscovite compared with the spectrum derived by threshold masking of high intensity pixels in the Al component map determined by spectral fitting of the Al 1s image sequence with muscovite.

particles of SiO_2 in this region of the biofilm and a very low level of the muscovite signal, but the majority of the signal detected is associated with the organo-silicate component. Spectra derived by threshold masking of the regions with high-intensity pixels in the muscovite, coesite and organo-silicon component maps are also shown in Fig. 8B, in comparison with the reference spectra. The spectrum extracted from intense pixels in the organo-silicate component map exhibits a broad, two-component peak with the lower component similar in energy to the main peak in the organo-silicon reference spectrum, and the higher energy component well matched to the peak of that in silicate minerals. It was not possible to divide the organo-silicate component map into regions where the ratio of these two peaks differed. This suggests that either this broad, approximately double-peaked signal was associated with a single compound, or there were two compounds, but for specific chemical reasons, they were always found together in a similar ratio. Note, the filamentous sheath and the immediate surrounding area were the dominant locations of this organo-silicate species. Figure 8F presents a color-coded composite map of the muscovite, organo-silicate and SiO_2 components. The bacterial sheaths have relatively uniform distributions of the organo-silicate. There are discrete particles of SiO_2 and muscovite in this region of the biofilm. The filamentous sheath and the immediate surrounding area are the dominant location of the organo-silicate species, and the organo-silicate was relatively uniformly distributed over the bacterial sheaths. Note that the majority of the Si signal detected is associated with the organo-silicate component. To quantify the organo-silicate, the chemical formula was assumed to be $\text{CSi}_2\text{O}_{10}\text{H}_{10}$ with a density of 3 g cm^{-3} . There was only about a 20% change in the quantitation result when the amount of Si or oxygen in the postulated chemical formula was doubled.

Aluminum

The distribution of Al in this region of the biofilm is displayed in Fig. 9. This was determined from the difference of the sum of images from 1555–1562 eV (pre-Al 1s) and the sum of images from 1565–1575 eV (Al 1s continuum). The Al occurred mostly as discrete particles that were not in direct association with the sheaths of the filamentous bacteria nor with the rod-shaped bacteria. A weak Al 1s signal was detected in the region of the filamentous sheaths. The Al 1s edge has been used to differentiate Al minerals (Ildefonso *et al.*, 1998; Yoon *et al.*, 2004). The Al 1s image sequence was fit using muscovite as the reference compound, which gave a component map that was very similar to that of the Al 1s image difference map. The spectrum derived by threshold masking the component map to select high-intensity pixels (region not shown) is plotted in Fig. 9B, in comparison with the Al 1s spectrum of muscovite. The two spectra are very similar, suggesting that muscovite, or a mineral with a similar local environment of the Al atom to that of muscovite, was present in this region of the biofilm.

Potassium

It is possible to differentiate K species using the K 2p-edge (Sette *et al.*, 1989; Hasselström *et al.*, 2000), specifically the multiplet structure of the $2p_{3/2} \rightarrow 3d$ and $2p_{1/2} \rightarrow 3d$ transitions depends strongly on the local environment in crystalline K species. The distribution of K in this region of the biofilm determined by spectral fitting is displayed in Fig. 2E. The spectrum derived by threshold masking regions with high intensity in the K component map is plotted in Fig. 3, in comparison with the spectrum of K in K_2CO_3 . Since there is no $\text{C } 1s \rightarrow \pi^*$ signal from carbonate at the point where the K signal was observed, it is clearly not K_2CO_3 but must be some other K-containing mineral, such as muscovite, and indeed there is a reasonable correlation of the position of the strong K signals with the Al-rich particles (Fig. 9).

A comparison of the distribution of K with the biology map (Fig. 1B) and protein, lipid and polysaccharide maps (Fig. 2) showed that K was not associated spatially with the rod-shaped bacterial cells, unbound EPS or with the sheaths of the filamentous bacteria.

Magnesium

The magnesium spectrum collected from a single particle in another part of the biofilm is presented in Fig. S2A. It was found to have a lineshape similar to that of cordierite and fosterite (Trcera *et al.*, 2008). The Mg 1s image difference map for the region of detailed study was measured and is displayed in Fig. S2B. There were a few discrete particles that contained Mg but neither the filamentous sheaths nor the rod-shaped bacteria sorbed Mg.

Elemental composition of the filamentous sheath

Clearly one of the most interesting aspects of these results is the relatively high concentration of several metal ion species on the sheath of the filamentous bacteria. On close examination of the maps (see, especially, the Ni map in Fig. 4 and the Mn(III) map in Fig. 5), the metal ions are not uniformly distributed but concentrated at the surface – if the metal ions were uniformly distributed through the filament one would expect to see a lower intensity at the edge whereas the metal ion signals are strongly enhanced at the edges. Although the analysis presented above tries to identify dominant chemical species (or at least oxidation states) from the fits to the NEXAFS spectra of specific compounds, it is also interesting to look at the compositional analysis of the filamentous sheaths from a purely elemental perspective. This has been carried out for those elements where full image sequences were recorded (C, O, Mn, Fe, Ni, Al and Si), by extracting the spectrum from isolated regions of the filamentous sheaths, and estimating the elemental content by the magnitude of the edge jump (i.e. without using the resonant signals, which are speciation-dependent). To quantify the amount of each element, we have matched the absorption edge jumps to the mass absorption coefficients of each element (Henke *et al.*, 1993), which thus gives the product of thickness and density, rather than just thickness, as is derived in our fit analysis. Figure 10 plots the measured spectra of the sheath in comparison with the sum of the elemental amounts deduced from this approach. The lower part of Fig. 10 plots the spectra of the individual edges along with the elemental edge jump signals (after background subtraction). The elemental amounts and approximate atomic percentages are summarized in Table 3. While the fit to the absorption over the 250- to 2000-eV range measured is not perfect, the general trends are reasonable, and the individual edge jumps can be quantified at the 10–30% level, and in large part are limited due to the measurement of too short energy ranges, rather than statistical precision. The overall result is also hampered by the absence of images sequences for the P

2p edge (too low to reach easily) and the Ca 2p edge (not measured due to oversight). Still, given the very small area being analyzed ($\sim 2 \mu\text{m}^2$), the result is considered significant and worthy of discussion.

One of the big surprises is that the most abundant elements found in the filamentous sheath are Si and O. In part, this may be a result of a low level of organic matter due to the absence of the bacteria, which made the sheath that left due to changing environmental conditions including the high local concentration of toxic Ni^{2+} (see below). Although this sheath cannot be linked to a specific organism, as that would require very specific morphology or molecular analyses, we think it is bacterial and not diatomaceous, because: (i) the Si content is well below that typical of diatoms which is $>95\% \text{SiO}_2$ (Dynes *et al.*, 2006b); (ii) diatom frustules are highly structured with striae and punctae, whereas the sheath was not ornamented and is associated with lipid; (iii) the scale of the filamentous structures ($<1/2 \mu\text{m}$ by a few micrometers) are consistent with bacteria or bacteria-like organisms; (iv) during the bio-reactor growth, a small amount of methanol was used to stimulate that biofilm growth and methanol is highly toxic to algae; (v) these sheaths appear to have developed during the reactor growth phase, and not to have been deposited from the water phase; (vi) scanning laser microscopy of this biofilm indicated that the sheath was not autofluorescent nor were any autofluorescent pigment (chlorophyll) bearing filaments observed; and (vii) sheath-like fine filamentous, non-fluorescent structures were also seen with lectin staining of the biofilm. There are various examples in the literature of bacterial sheaths, cell walls, etc. concentrating silica during life and after death (Toporski *et al.*, 2001; Konhauser, 2007)

The intense organo-silicon signal in the Si 1s spectrum (Fig. 10) suggests that the silica deposition is guided by the filament to form a porous 3d organo-silicon scaffold. This eventually converts to a more oxidized form and the combined 'organo-silicate' structure is the site of the metal adsorption. Konhauser (2007) outlines specific mechanisms for binding silicates to cell surfaces. The close spatial association with an initial organo-silicon environment with the more oxidized silicate environment conveniently rationalizes why we are not able to separate these two components in our fitting analysis of the Si 1s map.

Spatial relationship between Ni and selected metals

To show more explicitly the close spatial relationship of Ni, Mn, Fe, Ca and Si on the sheaths, color-coded composite maps overlaid on the biology map are presented in Fig. 11. This display clearly shows there is selective sorption of Ni by the filamentous sheaths and not by the rod-shaped bacteria. It also shows that the sheaths are very rich in metals (Mn, Fe, Ca and Si) relative to their surroundings, suggesting that the selectivity for the sheaths to sorb Ni was due, at least in part, to the presence of the Mn, Fe, Ca and/or Si sorbed on the sheaths.

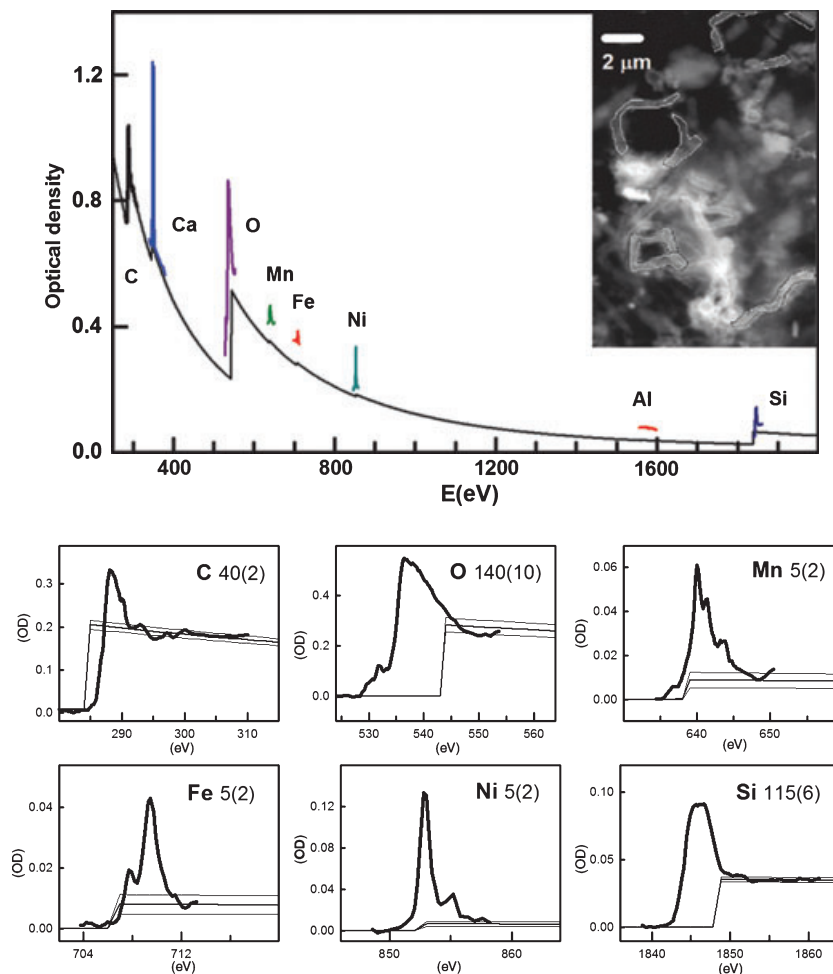


Fig. 10 Upper part: Optical density spectrum of the filamentous sheath in the C 1s, O 1s, Mn 2p, Fe 2p, Ni 2p, Al 1s and Si 1s edges, compared with the sum of the mass absorption coefficients in the amounts given in Table 3. The spectrum of Ca is that of $\text{Ca}(\text{H}_2\text{PO}_4)_2$ scaled to match the Ca edge jump, which was deduced from the signal in the filamentous sheath in the Ca map in Fig. 7. The insert is the sum of six images from 526 to 530 eV in the O 1s image sequence. The manually selected area defining the filamentous sheath is indicated. Lower part: Linear background subtracted spectra of the filamentous sheath at the C, O, Mn, Fe, Ni and Si edges, along with the elemental edge jump signals (and uncertainties) used to deduce the elemental amounts reported in the label and in Table 3.

DISCUSSION

This study has used STXM at a variety of absorption edges to map metal and organic species in a complex natural microbial biofilm grown in a model system that had been exposed to $10 \text{ mg L}^{-1} \text{ Ni}^{2+}$ for 24 h at the end of a 10-week incubation period. The results show that Ni was sorbed only on the sheaths of filamentous bacteria, which was also the location where high levels of Mn, Si, Ca and Fe were found. The Ni was not sorbed on the rod-shaped bacteria, unbound EPS or discrete particles of muscovite, SiO_2 and CaCO_3 . The sorption of the Mn, Si, Fe and Ca (bio)minerals, as discussed below, likely occurred prior to exposing the biofilm to Ni. We interpret these results to indicate that sorption to (bio)minerals already formed on these filamentous sheaths was the major reason for the selective adsorption of Ni in the biofilm. To put the Ni sorption in a proper perspective, the (bio)

mineralization within the sheath and the sheath organic sorption sites are discussed prior to discussing possible mechanisms of Ni sorption on to the sheaths and associated minerals.

Biominerals on the sheaths

The lack of a protein signal in the sheaths of the filamentous bacteria (Fig. 2A) indicated that they were devoid of bacterial cells, as cells contain roughly 50% protein (Ingraham *et al.*, 1983). One of the main functions of sheaths is to protect the cell from being encrusted by minerals, through the shedding of mineral-encased sheaths (Hallberg & Ferris, 2004; Phoenix & Konhauser, 2008), which may be the reason for the discarded sheaths in the biofilm. Another function is to protect cells from toxic species, including metals (Benning *et al.*, 2004). Ni is typically toxic at the 10 mg L^{-1} level towards

Table 3 Amounts of selected species in the filamentous sheath derived from fits to edge jumps

Edge	Mass absorption* (nm cm g ⁻¹)	μ/A	Atom % [†]	Comment
P	[35]	1.1	[6]	Indirect [‡]
S 2p	0 (5)	0	0	See Fig. S3
Cl 2p	[0]	0	0	See Figs S3 and S4
C 1s	40 (2)	3.3	18 (1)	
Ca 2p	10 (5)	0.25	1	From resonant peak
O 1s	140 (10)	8.8	49 (3)	
Mn 2p	5 (2)	0.09	0.5 (2)	
Fe 2p	5 (2)	0.09	0.5 (2)	
Ni 2p	5 (2)	0.08	0.5 (2)	
Na 1s	0 (2)	0	0	See Fig. S3
Mg 1s	0 (2)	0	0	See Fig. S3
Al 1s	3 (2)	0.11	0.6 (4)	
Si 1s	115 (6)	4.1	23 (1)	

*Since the image sequences were measured in slightly differing areas, manual identification of approximately the same region of the sheath was used. Care was taken not to include areas with a different morphology. It is considered that the errors from this approach are within the errors estimated from the match to the scaled elemental mass absorption coefficients (see the lower part of Fig. 10).

[†]This assumes the materials are all at unit density, which likely represents an under-estimation for the mineral component. Bold values are elements present at >10 atom%.

[‡]This amount of P as added to bring the pre-edge intensity below the C 1s onset in the sum of the elemental amounts in agreement with the pre-edge intensity in the C 1s spectrum of the sheath.

micro-organisms, thus it is possible that the sheaths were shed in response to the sorption of Ni (Phoenix & Konhauser, 2008). The experimental design employed in this study did not allow us to determine how the sheaths were discarded.

Mineral formation by microbes involves complex interactions between metal ions in solution and reactive components of the biofilm (Drews & Weckesser, 1982; Douglas &

Beveridge, 1998; De Yoreo & Vekilov, 2003). Metal ion binding to biological surfaces appears to be at least a two-step process. The first step is passive adsorption, whereby there is an electrostatic interaction between the metal ion and the surface reactive groups (e.g. carboxyl, phosphate) on the cell walls and/or outer external cell layers (e.g. EPS, sheath) (Weckesser *et al.*, 1988; Urrutia *et al.*, 1992). These surface functional groups are highly reactive towards metal ions on account of their amphoteric nature and low isoelectric point. The second step involves further metal deposition on the metal species initially bound to the surface, usually as a result of protonation and deprotonation reactions of surface hydroxyl or water groups (Miyata & Tazaki, 1997; Tazaki, 2000). With time and favorable thermodynamics, the process eventually leads to biomineral formation. Such biominerals are in turn capable of sorbing metal ions (Jackson *et al.*, 1999). On bacterial surfaces, there are a variety of negatively charged functional groups, including amino, carboxylic, hydroxyl and phosphate (Ferris *et al.*, 1987; Beveridge, 1989; Schultze-Lam *et al.*, 1992; Ledin *et al.*, 1999) that can serve as sites for sorption of metal cations. Also, some minerals carry a negative charge due to cation vacancies in oxide layers, as found in Mn(III) and Mn(IV) oxides (Lanson *et al.*, 2002; Saratovsky *et al.*, 2006; Villalobos *et al.*, 2006), or due to isomorphous substitution in, for example, phyllosilicates (Caillerie *et al.*, 1995), providing a driving force for cation sorption and intercalation. In addition to the negatively charged functional groups, bacterial surfaces also have groups with positive charges such as amino and amide groups that can serve as sorption sites for metal anions (e.g. SiO_3^{2-}) (Urrutia & Beveridge, 1993, 1994). Also, sorbed cations on bacterial surfaces can sorb anionic species (e.g. CO_3^{2-}), acting as cation bridges (Konhauser, 2007).

Thermodynamic equilibrium calculations using PHREEQC indicated that the Saskatchewan River water was super-

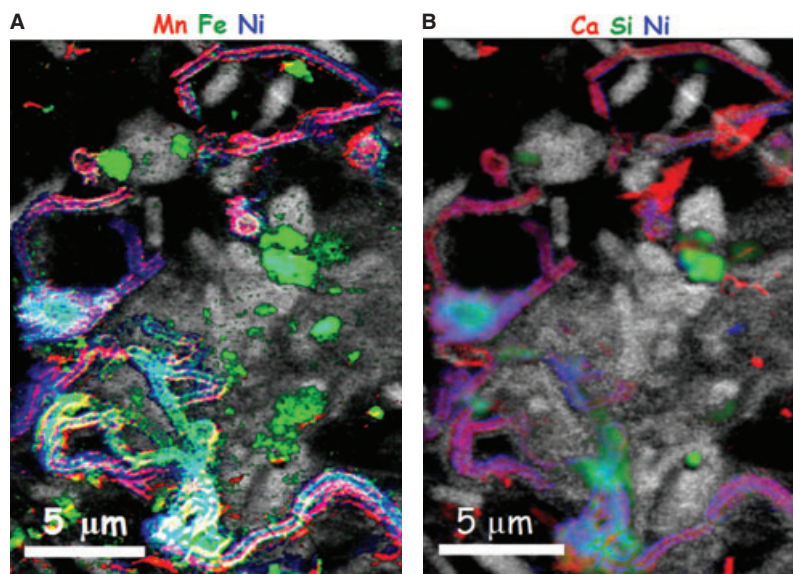


Fig. 11 Color-coded composite maps (individually rescaled) of (A) Mn, Fe and Ni derived from image difference maps (Figs 5A, 6A and 4A respectively), and (B) Ca, Si and Ni derived from image difference maps (Figs 8A, 7B and 4A respectively). All maps were superimposed on the biological map (C 1s image difference map, Fig. 1B).

saturated with respect to the following species; aragonite (CaCO_3), calcite (CaCO_3), hydroxyapatite [$\text{Ca}_5(\text{PO}_4)_3\text{OH}$], dolomite [$\text{CaMg}(\text{CO}_3)_2$], birnessite (MnO_2), bixbyite (Mn_2O_3), hausmannite (Mn_3O_4), manganite (MnOOH), gibbsite [$\text{Al}(\text{OH})_3$], diaspore (AlOOH), ferric hydroxides [$\text{Fe}(\text{OH})_3$], goethite (FeOOH), hematite (Fe_2O_3), magnetite (Fe_3O_4), $\text{Ni}(\text{OH})_2$ and Ni_2SiO_4 . Which species actually forms is of course a function of kinetic factors as well as thermodynamics, and the role of the microbes in bioaccumulation is played through their influence on the crystallization kinetics.

The sheaths of the filamentous bacteria in this study were found to bioaccumulate Mn species in the (II), (III) and (IV) oxidation states (Fig. 5). In natural waters, solid Mn(IV) oxides are ubiquitous (Shiller & Stephens, 2005). Toner *et al.* (2005) added $\text{Mn}^{2+}_{(\text{aq})}$ to *Pseudomonas putida* biofilms and observed that the Mn(II) was oxidized to solid Mn(III) and Mn(IV) oxides, which bioaccumulated on the bacterial surfaces. Many other laboratory studies have shown that $\text{Mn}^{2+}_{(\text{aq})}$ is oxidized by bacteria to Mn(III) and Mn(IV) oxides and bioaccumulated by bacterial surfaces (Bargar *et al.*, 2000; Pecher *et al.*, 2003; Jürgensen *et al.*, 2004; Tebo *et al.*, 2004). Generally, in those laboratory studies, there was a near-complete conversion of the $\text{Mn}^{2+}_{(\text{aq})}$ species to Mn(III) and Mn(IV) oxides, in contrast to this study, where a large amount of the Mn (40%) occurred in the Mn(II) oxidation state. The Mn concentration in solution was expected to be relatively constant for the entire 10-week growth period because the water was continually renewed (about 20% exchanged per day) as the bioreactor system was set up to simulate the adjacent river. Thus, there was a constant supply of Mn, presumably as $\text{Mn}^{2+}_{(\text{aq})}$ species, to the biofilm. Bargar *et al.* (2005) showed that Mn(II) could act as a reductant towards biogenic Mn(IV) oxides as it is readily sorbed by them (Adams & Ghiorse, 1988; Nelson *et al.*, 1999; Haack & Warren, 2003), resulting in mixed Mn oxidation (III, IV) products. This fact, and the continued exposure of the biofilm to $\text{Mn}^{2+}_{(\text{aq})}$ species, may account for our observations. Our results also provide evidence that Mn(III) and Mn(IV) (bio)minerals are formed in nature at low Mn concentrations ($0.4 \mu\text{M}$) (Fig. 5, Table 1); previous laboratory studies had shown the same phenomenon but Mn concentrations of $10 \mu\text{M}$ to 12mM were used (Bargar *et al.*, 2000, 2005; Villalobos *et al.*, 2003; Toner *et al.*, 2005).

Both Fe(II) and Fe(III) species were detected; however, Fe(III) was the dominant Fe species found on the sheaths. Ferric iron is known to bind tenaciously to bacterial surfaces and form insoluble biominerals (Konhauser, 1998; Warren & Ferris, 1998; Konhauser & Urrutia, 1999; Banfield *et al.*, 2000; Chan *et al.*, 2004). Thus, ferric oxyhydroxide formation on bacterial surfaces is widespread in nature, particularly in oxygenated environments (Konhauser & Urrutia, 1999). The ferric iron may originate from cell-bound ferrous iron (Châtellier *et al.*, 2004), where it undergoes oxidation and hydrolysis, a process recently studied using STXM and other

techniques by Miot *et al.* (2009). Other sources of Fe(III) include sorption of soluble ferric or colloidal species, or from the spontaneous oxidation of ferrous species that come into contact with oxygen, with the bacteria serving as the nucleation sites. The relatively large amount of ferric iron sorbed to the sheaths seems to preclude cell-bound ferrous iron as a significant source. The water used in this study was initially well oxygenated and remained as such in the rotating annular reactor. Thus, soluble ferric species should be present, although ferric colloidal species may dominate as the pH of South Saskatchewan River water was 8.5 (Ferris *et al.*, 1989a,b). Previous studies have demonstrated that bacterial surfaces bioaccumulate ferric species under acid conditions (Ferris *et al.*, 1989a,b; Warren & Ferris, 1998). However, at near-neutral pH bioaccumulation of Fe is much higher than at low pH. Under these oxygenated conditions, Fe(II) is expected to be readily oxidized to Fe(III) (Konhauser, 2007). In natural waters, Fe(II) can be stabilized through complexation with organic compounds (Theis & Singer, 1974), which may account for the presence of Fe(II) species in this region of the biofilm. Note that many rivers, including the South Saskatchewan river, receive anoxic groundwater containing organic chelated ferrous iron. Another possibility is that some of the Fe(II) species are stabilized in lower pH, or anoxic micro-environments, a situation that has been documented to occur in *Pseudomonas aeruginosa* biofilms (Hunter & Beveridge, 2005; Hunter *et al.*, 2008). In summary, it could not be determined whether the Fe(III) bioaccumulation by the sheath was from sorption of soluble Fe(III) species, colloidal Fe species, or by oxidation of Fe(II) species. Moreover, Fe is often associated with Mn as a ferromanganese [Mn(II), Fe(II)] precipitate in natural systems (Dean *et al.*, 1981; Konhauser, 2007), forming in an aerobic environment from the reduction of Mn(III), Mn(IV) and Fe(III) oxides bioaccumulated by cyanobacteria or algae. Tazaki (2000) examined natural microbial mats from river water using an electron microscope and observed that Fe–Mn oxides were sorbed only after the sorption of layer silicates. They proposed that bioaccumulated Mn(IV) oxides oxidize Fe(II) with a concomitant reduction to Mn(II), and that Fe(III) (ferrihydrate) was sorbed by the bacterial surfaces. Our observations appear to be consistent with this proposal since silicates were the dominant chemical component of the sheaths.

It has been proposed that aqueous silica is heterogeneously sorbed onto bacterial surface functional groups via three mechanisms: (i) hydrogen bonding, (ii) bonding to the positively charged functional groups and (iii) cation bridging (Urrutia & Beveridge, 1993; Schultze-Lam *et al.*, 1995; Westall *et al.*, 1995; Jones *et al.*, 1997; Konhauser, 2007; Peng *et al.*, 2007). Urrutia & Beveridge (1993, 1994) showed that Fe pretreatment of bacterial cells at pH 8 enhanced the binding of silicate, whereas at acidic values silicate was more favorably bound when the cells were not treated with Fe. Similar results have been obtained by other

researchers (Scheidegger *et al.*, 1993; Manceau *et al.*, 1995; Fortin *et al.*, 1998; Fein *et al.*, 2002). Under such conditions, Konhauser & Urrutia (1999) suggested that Fe sorbs to the bacterial surfaces followed by Si and Al sorption. In this study, the pH of the river water was 8.5, and Fe(III) was sorbed by the sheath. From the analysis of the Si 1s image sequence (Fig. 8) and the detailed elemental analysis (Fig. 10), it is evident that the organo-silicate component dominated the composition of the sheath of the filamentous bacteria. The presence of the organosilicon spectroscopic signal indicates that a C–O–Si bond was present. Heinen (1965) used IR to study the interaction of Si with the bacteria *Proteus mirabilis* and also observed C–O–Si signals.

Ca²⁺ was bioaccumulated by the sheaths (Fig. 7), but there was relatively little carbonate (Fig. 2D). CaCO₃ minerals are ubiquitous in nature (Riding, 2000; Braissant *et al.*, 2003; Dittrich & Obst, 2004; Benzerara *et al.*, 2006). It is well known that micro-organisms, particularly cyanobacteria, facilitate carbonate precipitation by the adsorption of Ca²⁺ cations to their cell surfaces and photosynthetic uptake of HCO₃⁻ and the concomitant release of OH⁻ under limited CO₂ supply (Obst *et al.*, 2006, 2009; Ercole *et al.*, 2007; Lalonde *et al.*, 2007a). That is, Ca²⁺ acts as a cation bridge between the negatively charged functional groups on the bacterial surface and the carbonate anion. The amount of Ca²⁺ on the sheath was much higher than the amount of carbonate. Obst *et al.* (2009) have shown that Ca²⁺ is sorbed by planktonic cyanobacteria cells on surface EPS. Aragonite-like CaCO₃ was then nucleated and grown from the adsorbed Ca²⁺, and both co-existed on the cyanobacterial surface. Therefore, in this study, it is likely that both CaCO₃ and adsorbed Ca²⁺ were present on the sheaths. Note that the formation of siderite (FeCO₃) and rhodochrosite (MnCO₃) was unlikely to have occurred in our system as these minerals usually form in anaerobic environments in the presence of microbes (Konhauser, 2007).

Although small, there was some Al detected on the sheaths. The low level of Al was surprising since Al-silicates are ubiquitous in natural environments (Konhauser *et al.*, 1993, 1994; Konhauser & Urrutia, 1999; Peng *et al.*, 2007). The fact that the aqueous Al concentration (5–20 µg L⁻¹) in this study was 1–2 orders of magnitude lower than that of the other natural freshwater systems studied (Konhauser *et al.*, 1993, 1994) may account for the low levels of Al in the biomineralized sheaths. The concentration of Mg (Table 1) in the natural water was significantly larger than most of the other metals, except Ca; however, it was not sorbed by the sheaths or the rod-shaped bacteria. This is attributed to the fact that Mg²⁺ is very soluble, i.e. it prefers to bind to a water molecule rather than a phosphate or carboxylate oxyanion (Collins, 2006).

Ni sorption

Even though all of the biofilm components were exposed simultaneously to Ni under the same environmental condi-

tions, the natural river biofilm selectively sorbed Ni only on the sheaths of the filamentous bacteria. Ni sorption was not apparent on the rod-shaped bacteria, the unbound EPS or on the discrete mineral particles (i.e. muscovite, SiO₂, CaCO₃). This stark contrast in Ni sorption capabilities by the various components led us to examine and compare the biochemistry and mineralogy of these components to understand the Ni sorption processes taking place in the biofilm. In solution, simple Ni²⁺ salts immediately dissociate to [Ni(OH₂)₆]²⁺ with the original ligands acting as non-coordinating or weakly coordinating counter-anions (Richens, 1997). STXM showed that the Ni species that sorbed to the sheath in this study was in the +2 oxidation state (Fig. 4), confirming that the Ni²⁺ cation was sorbed without oxidation or reduction. Bacterial surfaces have negatively charged surface functional groups that could serve as sites for adsorbing Ni²⁺ (Beveridge & Murray, 1980; Sar *et al.*, 1999; Konhauser, 2007). Ni adsorption by the cell wall of a pure culture of the cyanobacteria *Anabaena cylindrica* has been demonstrated (Campbell & Smith, 1986). Our results (Figs 5–8 and 11) indicate that extensive (bio)mineralization on the sheath had occurred with a strong preference to the sheath surface. Jackson *et al.* (1999), studying Cu adsorption on benthic communities, not only showed that blockage of cell wall ligands by Si-, Al- and Fe-bearing mineral deposits occurs but also showed extensive sorption of Cu by the cell walls, although the sorption was weaker than that observed for the mineral phases. Other researchers (Beveridge & Murray, 1980; Doyle *et al.*, 1980) studying pure bacterial cultures have shown that the introduction of positive charges into cell walls and/or alteration of the charge on carboxyl groups (making them neutral or electropositive) resulted in a decrease in the number of metal-binding sites, thus severely limiting metal sorption onto bacterial surface anionic groups. Templeton *et al.* (2001, 2003) used the long-period X-ray standing wave technique to probe the sorption of Pb²⁺ by *Burkholderia cepacia* biofilms formed on mineral surfaces (e.g. α-Al₂O₃, α-Fe₂O₃). At low-Pb concentrations (~200 µg L⁻¹), the reactive sites on the metal oxides were not passivated by the formation of the biofilm. That is, Pb was preferentially sorbed by the mineral surfaces rather than the biofilm surfaces. When the Pb concentration was increased tenfold, Pb was also sorbed by the biofilm surfaces. In our system, the sheaths were encrusted by the biominerals, whereas in the Templeton *et al.*'s system the minerals were covered by the biofilm. Thus, it may be expected that the biominerals were the preferred sorption sites. However, the Ni concentration used in this study was high (10 mg L⁻¹), thus sorption to the surface groups on the sheath probably occurred. Nevertheless, even at this high Ni concentration, Ni sorption by the rod-shaped bacteria was not observed. In the case of the rod-shaped bacteria, the type and abundance of their surface anionic functional groups may have been significantly different than those on the

sheath surface, so as to exclude Ni sorption (Konhauser, 2007).

We believe that the (bio)mineral(s) that formed on the sheaths prior to the addition of Ni were a major site for Ni sorption. Adsorption of bivalent metal ions on metals oxides has been documented (Tamura & Furuichi, 1997). The sheaths were encrusted by a number of metal species/(bio)minerals (Figs 5–8), all of which may have served as Ni sorption sites on the sheath. Note, however, that co-localization does not necessarily imply chemical interaction between Ni and the metals/(bio)minerals. The Ni–Mn color composite map (Fig. 11A) shows very clearly that the Ni and Mn distributions were very similar. Mn species occurred on the sheath as Mn(II), Mn(III) and Mn(IV) species (Fig. 5). Biogenic manganese oxides (Mn^{+4}) are known to bioaccumulate many metals, including Ni (Tani *et al.*, 2004; Tebo *et al.*, 2004). Villalobos *et al.* (2005) indicated that organic sorption sites in biofilms do not appear to compete effectively with Mn(IV) oxides in scavenging trace metals such as Pb(II) and Mn(II). This observation may also be applicable to Ni^{2+} . Ni^{2+} adsorption on MnO_2 was shown to occur above pH 4, with maximum adsorption at pH > 7 (Tamura & Furuichi, 1997). In this system, the pH of the water was 8.5; thus, there should have been ample Mn(III) and Mn(IV) oxide sites available for Ni sorption. Besides these pH-dependent sites, Mn(III) and Mn(IV) oxides also carry a negative charge due to cation vacancies in the oxide layers (Saratovsky *et al.*, 2006), and these sites appear to be favorable for Ni sorption. The extent of Ni(II) substitution for Mn(II) in manganese oxides is extremely limited (Kay *et al.*, 2001); thus, it is unlikely that Ni substituted for Mn(II) in the oxides. Rather, we believe that Ni was adsorbed to the Mn(III) and Mn(IV) oxide biominerals on the sheath. Moreover, it was observed that Zn^{2+} sorption to the organic sites only occurred after depletion of the Mn sorption sites on the Mn(IV) oxides (Toner *et al.*, 2006), supporting the contention that Ni has a preference for Mn over organic sorption sites. In addition, biogenic Mn oxides showed about tenfold higher efficiency than synthetic Mn oxides ($\gamma\text{-MnO}_2$) for sorbing Ni^{2+} , and also had higher irreversibility of Ni sorption on biogenic Mn oxides (Tani *et al.*, 2004). The amount of Ni sorbed appears to be large compared with the amount of Mn(IV) oxides, which may be due to the formation of a Ni biomineral or that Ni was sorbed on other sites.

Fe(III) species were also present on the sheaths of the filamentous bacteria (Fig. 6). Ni^{2+} sorption by ferric minerals (e.g. hydrous ferric oxides, goethite) was 100% at pH > 7 (Fischer *et al.*, 2007; Xu *et al.*, 2007). At pH 8.5, the ferric iron species on the sheaths are expected to be deprotonated, thus Ni sorption was also likely on Fe(III) species on the sheaths.

The organo-silicate dominates the chemistry of the sheath (Fig. 8). Silica has been shown to adsorb Ni from solution (Xu & Axe, 2005). In the environment silica is often associated

with iron oxides. Xu & Axe (2005) also showed that goethite coated with silica adsorbed Ni, and that both the silica and goethite surfaces were available for Ni adsorption. In fact, Ni sorption was greater on the goethite silica-coated material than on the sum of goethite and silica, apparently due to a change in the goethite-coated silica surface properties vs. that of the goethite and silica themselves. Hence, Ni sorption was also likely on organo-silicate species on the sheath.

Muscovite is a non-expandable clay, thus ion exchange is limited to the surface ions, i.e. the potassium and sodium ions in the interlayers are not exchangeable under ambient conditions (Osman *et al.*, 1998). The muscovite in this study sorbed Fe(III), K^+ and Ca^{2+} but the number of surface sites were apparently too low to result in significant Ni adsorption, and/or the sorbed cations were not readily exchangeable, or the effective Ni concentration was too low due to sorption to the other biominerals on the sheaths.

CONCLUSIONS

Scanning transmission X-ray microscopy combines high spatial resolution with speciation and quantitative mapping of metal and major biomacromolecules, based on reasonably well-understood X-ray absorption spectroscopy. This enables detection, identification and quantitative mapping of metal species on individual microbial species in complex natural biofilms, which in turn has provided useful insight into Ni sorption processes. In the mixed microbial species biofilm examined in this study, Ni was selectively sorbed on organo-silicate-rich sheaths of filamentous bacteria. This was attributed to the presence of Mn, Fe and Si minerals on the sheaths. Thus, the fate and effects of Ni ions in aquatic ecosystems are intimately linked to that of Mn(II), Mn(III) and Mn(IV) oxides, Fe(III) hydroxides/oxides, as well as silicates bioaccumulated on particular species in biofilms and the availability of suitable sorption sites at the microscale. This specificity with regard to Ni sorption demonstrates that Ni distributions, mobility and bioavailability in natural systems can be influenced by a few select microbial species. Also, this work highlights the complexity of natural systems in that sorption sites on microbes may be occupied by previously sorbed metals or mineral phases. Thus, some of the experimental work on individual species in controlled solutions may not be applicable to natural systems. Studies in natural systems are critical to understanding the role of microbes in mineralization processes. These results may have implications with regard to bio-amplification in the food chain as toxic metal ions such as Ni^{2+} may be concentrated in specific microbial species, which might be preferential food sources for higher organisms. Furthermore, our results suggest that, if the microbial species responsible for the filamentous sheath formation could be isolated and cultured, they could be used to treat Ni-contaminated sites, which are a significant environmental problem.

ACKNOWLEDGEMENTS

This work was supported by Environment Canada, the Advanced Foods and Materials Network, NSERC (Canada), and the Canada Research Chair program (APH). Construction and operation of the STXM 5.3.2 and 11.0.2 microscopes are supported by NSF DMR-9975694, DOE DE-FG02-98ER45737, Dow Chemical, NSERC and the Canada Foundation for Innovation. We thank David Kilcoyne for his contributions to developing and maintaining the instruments. The Advanced Light Source is supported by the Director, Office of Energy Research, Office of Basic Energy Sciences, Materials Sciences Division of the U.S. Department of Energy, under Contract No. DE-AC03-76SF00098. We would like to thank the editor and reviewers whose many constructive comments helped improve the manuscript.

REFERENCES

- Adams LF, Ghiorse WC (1988) Oxidation state of Mn in the Mn oxide produced by *Leptothrix discophora* SS-1. *Geochimica et Cosmochimica Acta* **52**, 2073–2076.
- Banfield JF, Welch SA, Zhang H, Ebert TT, Penn RL (2000) Aggregation-based crystal growth and microstructure development in natural iron oxyhydroxide biomineralization products. *Science* **289**, 751–754.
- Bargar JR, Tebo BM, Villinski JE (2000) In situ characterization of Mn(II) oxidation by spores of the marine *Bacillus* sp. strain SG-1. *Geochimica et Cosmochimica Acta* **64**, 2775–2778.
- Bargar JR, Tebo BM, Bregmann U, Webb SM, Glatzel P, Chiu VQ, Villalobos M (2005) Biotic and abiotic products of Mn(II) oxidation by spores of the marine *Bacillus* sp. strain SG-1. *American Mineralogist* **90**, 143–154.
- Benning LG, Phoenix VR, Yee N, Tobin MJ (2004) Molecular characterization of cyanobacteria silicification using synchrotron infrared micro-spectroscopy. *Geochimica et Cosmochimica Acta* **68**, 729–741.
- Benzerara K, Yoon TH, Tyliczszak T, Constantz B, Spormann AM, Brown GE Jr (2004) Scanning transmission X-ray microscopy study of microbial calcification. *Geobiology* **2**, 249–259.
- Benzerara K, Menguy N, Lopez-Garcia P, Yoon T-H, Kazmierczak J, Tyliczszak T, Guyot F, Brown GE Jr (2006) Nanoscale detection of organic signatures in carbonate microbialites. *Proceedings of the National Academy of Sciences of the USA* **103**, 9440–9445.
- Beveridge TJ (1989) Role of cellular design in bacterial metal accumulation and mineralization. *Annual Review of Microbiology* **43**, 147–171.
- Beveridge TJ, Murray RGE (1980) Sites of metal deposition in the cell wall of *Bacillus subtilis*. *Journal of Bacteriology* **141**, 876–887.
- Bluhm H, Andersson K, Araki T, Benzerara K, Brown GE, Dynes JJ, Ghosal S, Gilles MK, Hansen H-Ch, Hemminger JC, Hitchcock AP, Ketteler G, Kneedler E, Lawrence JR, Leppard GG, Majzlam J, Mun BS, Myneni SCB, Nilsson A, Ogasawara H, Ogletree DF, Pecher K, Salmeron M, Tonner B, Tyliczszak T, Yoon TH, Shuh DK (2005) Soft X-ray microscopy and spectroscopy at the Molecular Environmental Science Beamline at the Advanced Light Source. *Journal Electron Spectroscopy and Related Phenomena* **150**, 86–104.
- Braissant O, Cailleau G, Dupraz C, Verrecchia EP (2003) Bacterially induced mineralization of calcium carbonate in terrestrial environments: the role of exopolysaccharides and amino acids. *Journal of Sedimentary Research* **73**, 485–490.
- Branda SS, Vik Å, Friedman L, Kolter R (2005) Biofilms: the matrix revisited. *Trends in Microbiology* **13**, 20–26.
- Brandes JA, Lee C, Wakeham S, Peterson M, Jacobsen C, Wirick S, Cody G (2004) Examining marine particulate organic matter at sub-micron scales using scanning transmission X-ray microscopy and carbon X-ray absorption near edge structure spectroscopy. *Marine Chemistry* **92**, 107–121.
- Caillierie JB, Gruver V, Fripiat JJ (1995) Modification of the surface properties of natural phyllosilicate sepiolite by secondary isomorphous substitution. *Journal of Catalysis* **151**, 420–430.
- Campbell PM, Smith GD (1986) Transport and accumulation of nickel ions in the cyanobacterium *Anabaena cylindrical*. *Archives of Biochemistry and Biophysics* **244**, 470–477.
- Chan CS, De Stasio G, Welch SA, Girasole M, Frazer BH, Nesterova MV, Fakra S, Banfield JF (2004) Microbial polysaccharides template assembly of nanocrystal fibers. *Science* **303**, 1656–1658.
- Châtellier X, West MM, Rose J, Fortin D, Leppard GG, Ferris FG (2004) Characterization of iron-oxides formed by oxidation of ferrous ions in the presence of various bacterial species and inorganic ligands. *Geomicrobiology Journal* **21**, 99–112.
- Chen CT, Sette F (1990) High-resolution soft X-ray spectroscopies with the Dragon beamline. *Physical Scripta* **31**, 119–126.
- Collins KD (2006) Ion hydration: implications for cellular function, polyelectrolytes, and protein crystallization. *Biophysical Chemistry* **119**, 271–281.
- De Yoreo JJ, Vekilov PG (2003) Principles of crystal nucleation and growth. *Reviews in Mineralogy and Geochemistry* **54**, 57–93.
- Dean WE, Moore WS, Neelson KH (1981) Manganese cycles and the origin of manganese nodules, Oneida Lake, New York, USA. *Chemical Geology* **34**, 53–64.
- Dittrich M, Obst M (2004) Are picoplankton responsible for calcite precipitation in lakes? *Ambio* **33**, 559–564.
- Douglas S, Beveridge TJ (1998) Mineral formation by bacteria in natural microbial communities. *FEMS Microbiology Ecology* **26**, 79–88.
- Doyle RJ, Matthews TH, Streips UN (1980) Chemical basis for selectivity of metal ions by the *Bacillus subtilis* cell wall. *Journal of Bacteriology* **143**, 471–480.
- Drews G, Weckesser J (1982) Function, structure and composition of cell walls and external layers. In *The Biology of Cyanobacteria* (eds Carr NG, Whitton BA). Blackwell Scientific Publications, Oxford, UK, pp. 333–357.
- Dynes JJ, Tyliczszak T, Araki T, Lawrence JR, Swerhone GDW, Leppard GG, Hitchcock AP (2006a) Speciation and quantitative mapping of metal species in microbial biofilms using scanning transmission X-ray microscopy. *Environmental Science and Technology* **40**, 1556–1565.
- Dynes JJ, Lawrence JR, Korber DR, Swerhone GDW, Leppard GG, Hitchcock AP (2006b) Quantitative mapping of chlorhexidine in natural river biofilms. *Science of the Total Environment* **369**, 369–383.
- van Elp J, Peng G, Searle BG, Mitra-Kirtley S, Huang Y-H, Johnson MK, Zhou ZH, Adams MWW, Maroney MJ, Cramer SP (1994) Electronic structure and symmetry in nickel L edge x-ray absorption spectroscopy: application to a nickel protein. *Journal of the American Chemical Society* **116**, 1918–1923.
- Ercolo C, Cacchio P, Botta AL, Centi V, Lepidi A (2007) Bacterially induced mineralization of calcium carbonate: the role of exopolysaccharides and capsular polysaccharides. *Microscopy and Microanalysis* **13**, 42–50.

- Fein JB, Scott S, Rivera N (2002) The effect of Fe on Si adsorption by *Bacillus subtilis* cell walls: insights into non-metabolic bacterial precipitation of silicate minerals. *Chemical Geology* **182**, 265–273.
- Ferris FG, Fyfe WS, Beveridge TJ (1987) Bacteria as nucleation sites for authigenic minerals in a metal-contaminated lake sediment. *Chemical Geology* **63**, 225–232.
- Ferris FG, Tazaki K, Fyfe WS (1989a) Iron oxides in acid mine drainage environments and their association with bacteria. *Chemical Geology* **74**, 321–330.
- Ferris FG, Schultze S, Witten TC, Fyfe WS, Beveridge TJ (1989b) Metal interactions with microbial biofilms in acidic and neutral pH environments. *Applied and Environmental Microbiology* **55**, 1249–1257.
- Fischer L, Brümmer GW, Barrow NJ (2007) Observations and modeling of the reactions of 10 metals with goethite; adsorption and diffusion processes. *European Journal of Soil Science* **58**, 1304–1315.
- Fortin D, Ferris FG, Scott SD (1998) Formation of Fe-silicates and Fe-oxides on bacterial surfaces in samples collected near hydrothermal vents on the Southern Explorer in the northeast Pacific Ocean. *American Mineralogist* **83**, 1399–1408.
- Grush MM, Chen J, Stemmler TL, George SJ, Ralston CY, Stibrany RT, Gelasco A, Christou G, Gorun SM, Penner-Hahn JE, Cramer SP (1996) Manganese L-edge X-ray absorption spectroscopy of manganese catalase from *Lactobacillus plantarum* and mixed valence manganese complexes. *Journal of the American Chemical Society* **118**, 65–69.
- Haack EA, Warren LA (2003) Biofilm hydrous manganese oxyhydroxides and metal dynamics in acid rock drainage. *Environmental Science and Technology* **37**, 4138–4147.
- Hallberg R, Ferris FG (2004) Biomineralization by *Gallionella*. *Geomicrobiology Journal* **21**, 325–330.
- Hall-Stoodley L, Costerton JW, Stoodley P (2004) Bacterial biofilms: from the natural environment to infectious diseases. *Nature Reviews* **2**, 95–108.
- Hasselström J, Föhlisch A, Denecke R, Nilsson A, de Groot FMF (2000) Crystal-field splitting in coadsorbate systems: $\alpha(2 \times 2)$ CO/K/Ni(100). *Physical Review B* **62**, 192–196.
- Heinen W (1965) Siliciumstoffwechsel bei Mikroorganismen, VII. Verteilung der Kieselsäure in Zell-Fractionen von *Proteus mirabilis* und der Nachweis von Kohlenhydrat-Kieselsäure-Esthem. *Archiv of Microbiology* **52**, 69–79.
- Henke BL, Gullikson EM, Davis JC (1993) Atomic scattering factors for the elements. *Atomic Data Nuclear Data Tables* **54**, 181–297.
- Himpel FJ, Karlsson UO, McLean AB, Terminello LJ, Degroot FMF, Abbate M, Fuggle JC, Yarmoff JA, Thole BT, Sawatzky GA (1991) Fine-structure of the Ca 2p X-ray-absorption edge for bulk compounds, surfaces, and interfaces. *Physical Review B* **43**, 6899–6907.
- Hitchcock AP (2008) aXis2000 is written in Interactive Data Language (IDL). It is available free for non-commercial use from <http://unicorn.mcmaster.ca/aXis2000.html> (last accessed on 15 July 2009).
- Hunter RC, Beveridge TJ (2005) Application of a pH-sensitive fluoroprobe (C-SNARF-4) for pH microenvironment analysis in *Pseudomonas aeruginosa* biofilms. *Applied and Environmental Microbiology* **71**, 2501–2510.
- Hunter RC, Hitchcock AP, Dynes JJ, Obst M, Beveridge TJ (2008) Mapping the speciation of iron minerals in *Pseudomonas aeruginosa* biofilms using scanning transmission x-ray microscopy. *Environmental Science and Technology* **42**, 8766–8772.
- Ildofones P, Cabaret D, Sainctavit P, Calas G, Flank AM, Lagarde P (1998) Aluminum X-ray absorption near edge structure in model compounds and earth's surface minerals. *Physics and Chemistry of Minerals* **25**, 112–121.
- Ingraham JL, Maaloe O, Neidhardt FC (1983) *Growth of the Bacterial Cell*. Sinauer Associates Inc., Sunderland, MA, pp. 1–48.
- Jackson TA, West MM, Leppard GG (1999) Accumulation of heavy metals by individually analyzed bacterial cells and associated nonliving material in polluted lake sediments. *Environmental Science and Technology* **33**, 3795–3801.
- Jones B, Renaut RW, Rosen MR (1997) Biogenicity of silica precipitation around geysers and hot-spring vents, North Island, New Zealand. *Journal of Sedimentary Research* **67**, 88–104.
- Jürgensen A, Widmeyer JR, Gordon RA, Bendell-Young LI, Moore MM, Crozier ED (2004) The structure of the manganese oxide on the sheath of the bacterium *Leptotrix discophora*: An XAFS study. *American Mineralogist* **89**, 1110–1118.
- Kay JT, Conklin MH, Fuller CC, O'Day PA (2001) Processes of Nickel and Cobalt uptake by a manganese oxide forming sediment in Pinal creek, globe mining district, Arizona. *Environmental Science & Technology* **35**, 4719–4725.
- Kilcoyne ALD, Steele WF, Fakra S, Hitchcock P, Franck K, Anderson E, Harteneck B, Rightor EG, Mitchell GE, Hitchcock AP, Yang L, Warwick T, Ade H (2003) Interferometrically controlled scanning transmission microscopes at the Advanced Light Source. *Journal of Synchrotron Radiation* **10**, 125–136.
- Konhauser KO (1998) Diversity of bacterial iron mineralization. *Earth-Science Reviews* **43**, 91–121.
- Konhauser KO (2007) *Introduction to Geomicrobiology*. Blackwell Publications, Oxford, UK, pp. 1–425.
- Konhauser KO, Urrutia MM (1999) Bacterial clay authigenesis: a common biochemical process. *Chemical Geology* **161**, 399–413.
- Konhauser KO, Fyfe WS, Ferris FG, Beveridge TJ (1993) Metal sorption and mineral precipitation by bacteria in two Amazonian river systems: Rio Solimoes and Rio Negro, Brazil. *Geology* **21**, 1103–1106.
- Konhauser KO, Schultze-Lam S, Ferris FG, Fyfe WS, Longstaffe FJ, Beveridge TJ (1994) Mineral precipitation by epilithic biofilms in the Speed River, Ontario, Canada. *Applied Environmental Microbiology* **60**, 549–553.
- Krasnikov SA, Preobrajenski AB, Sergeeva NN, Brzhezinskaya MM, Nesterov MA, Cafolla AA, Senge MO, Vinogradov AS (2007) Electronic structure of Ni(II) porphyrins and phthalocyanine studied by soft X-ray absorption spectroscopy. *Chemical Physics* **332**, 318–324.
- van der Laan G, Zaanen J, Sawatzky GA, Karnatak R, Esteva J-M (1985) Correlation effects, charge-transfer energies and covalency in nickel compounds as determined by x-ray absorption spectroscopy. *Solid State Communications* **56**, 673–676.
- van der Laan G, Zanene J, Sawatzky GA, Karnatak R, Esteva JM (1986) Comparison of X-ray absorption with X-ray photoemission of Nickel dihalides and NiO. *Physical Review B* **33**, 4253–4263.
- Lalonde SV, Amskold LA, Warren LA, Konhauser KO (2007a) Surface chemical reactivity and metal adsorptive properties of natural cyanobacterial mats from an alkaline hydrothermal spring, Yellowstone National Park. *Chemical Geology* **243**, 36–52.
- Lalonde SV, Konhauser KO, Amskold L, McDermott T, Inskip BP (2007b) Chemical reactivity of microbe and mineral surfaces in hydrous ferric oxide depositing hydrothermal springs. *Geobiology* **5**, 219–234.
- Lanson B, Drits VA, Gaillot AC, Silvester EJ, Plancon A, Manceau A (2002) Structure of heavy metal sorbed birnessite. 1. Results from X-ray diffraction. *American Mineralogist* **87**, 1631–1645.
- Lawrence JR, Swerhone GDW, Neu TR (2000) Design and evaluation of a simple rotating annular reactor for replicated

- biofilm studies. *Journal of Microbiological Methods* **42**, 215–224.
- Lawrence JR, Korber DR, Wolfaardt GM, Caldwell DE, Neu TR (2002a) Analytical imaging and microscopy techniques. In *Manual of Environmental Microbiology*, 2nd edn (eds Hurst CJ, Crawford RL, Knudsen GR, McInerney M, Stetzenbach LD). American Society for Microbiology Press, Washington, DC, pp. 39–61.
- Lawrence JR, Scharf B, Packroff G, Neu TR (2002b) Microscale evaluation of the effects of grazing by invertebrates with contrasting feeding modes on river biofilm architecture and composition. *Microbial Ecology* **44**, 199–207.
- Lawrence JR, Swerhone GDW, Leppard GG, Araki T, Zhang X, West MM, Hitchcock AP (2003) Scanning transmission X-ray, laser scanning, and transmission electron microscopy mapping of the exopolymeric matrix of microbial biofilms. *Applied Environmental Microbiology* **69**, 5543–5554.
- Lawrence JR, Chenier MR, Roy R, Beamier D, Fortin N, Swerhone GDW, Neu TR, Greer CW (2004) Microscale and molecular assessment of impacts of nickel, nutrients and oxygen level on structure and function of river biofilm communities. *Applied and Environmental Microbiology* **70**, 4326–4339.
- Ledin M, Krantz-Rülcker C, Allard B (1999) Microorganisms as metal sorbents: comparison with other soil constituents in multi-compartment systems. *Soil Biology and Biochemistry* **31**, 1639–1648.
- Li D, Bancroft GM, Kasrai M, Fleet ME, Feng XH, Tan KH, Yang BX (1993) High-resolution Si K- and L_{2,3}-edge XANES of α -quartz and stishovite. *Solid State Communication* **87**, 613–617.
- Li D, Bancroft GM, Kasrai M, Fleet ME, Secco RA, Feng XH, Tan KH, Yang BX (1994) X-ray absorption spectroscopy of silicon dioxide (SiO₂) polymorphs: the structural characterization of opal. *American Mineralogist* **79**, 622–632.
- Li D, Bancroft GM, Fleet ME, Feng XH (1995) Silicon K-edge XANES spectra of silicate minerals. *Physics and Chemistry of Minerals* **22**, 115–122.
- Manceau A, Ildefonse PH, Hazemann J-L, Flank A-M, Gallup D (1995) Crystal chemistry of hydrous iron silicate scale deposits at the Salton sea geothermal field. *Clays and Clay Minerals* **43**, 304–317.
- Miot J, Benzerara K, Morin G, Kappler A, Bernard S, Obst M, Ferard C, Skouri-Panet F, Guigner JM, Posth N, Galvez M, Brown GE Jr, Guyot F (2009) Iron biomineralization by anaerobic neutrophilic iron-oxidizing bacteria. *Geochimica et Cosmochimica Acta* **73**, 696–711.
- Miyata N, Tazaki K (1997) Biomineralization of layer silicates and hydrated Fe/Mn oxides in microbial mats: an electron microscopic study. *Clays and Clay Minerals* **45**, 203–212.
- Naftel SJ, Sham TK, Yiu YM, Yates BW (2001) Calcium L-edge XANES study of some calcium compounds. *Journal of Synchrotron Radiation* **8**, 255–257.
- Neal AL, Dublin SN, Taylor J, Bates DJ, Burns JL, Apkarian R, Di-Christina TJ (2007) Terminal electron acceptors influence the quantity and chemical composition of capsular exopolymers produced by anaerobically growing *Shewanella* spp. *Biomacromolecules* **8**, 166–174.
- Nelson YM, Lion LW, Ghiorse WC, Shuler ML (1999) Production of biogenic Mn oxides by *Leptothrix discophora* SS-1 in a chemically defined growth medium and evaluation of their Pb adsorption characteristics. *Applied and Environmental Microbiology* **65**, 175–180.
- Neu TR, Lawrence JR (2008) Extracellular polymeric substances in microbial biofilm systems. In *Microbial Glycobiology, Structures, Relevance and Applications Life Sciences*, Chapter 37 (eds Moran A, Brennan P, Holst O, von Itzstein M). Elsevier, San Diego, CA, pp. 735–758.
- Obst M, Ditttrich M, Kuehn H (2006) Calcium adsorption and changes of the surface microtopography of cyanobacteria studied by AFM, CFM, and TEM with respect to biogenic calcite nucleation. *Geochemistry Geophysics Geosystems* **7**, 1–15.
- Obst M, Dynes JJ, Lawrence JR, Swerhone GDW, Karunakaran C, Kaznatcheev K, Benzerara K, Tylliszczak T, Hitchcock AP (2009) Precipitation of amorphous CaCO₃ (aragonite) controlled by cyanobacteria: a multi-technique study of the influence of EPS on the nucleation process. *Geochimica et Cosmochimica Acta* **73**, 4180–4198.
- Osman MA, Caseri WR, Suter UW (1998) Ion exchange on muscovite mica with ultrahigh surface area. *Journal of Colloid and Interface Science* **198**, 157–163.
- Parkhurst DL, Appelo CAJ (1999) User's guide to PHREEQC (Version 2) – a computer program for speciation, batch-reaction, one-dimensional transport, and inverse geochemical calculations: U.S. Geological Survey Water-Resources Investigations Report 99-4259, pp. 1–312. Available at http://wwwbr.cr.usgs.gov/projects/GWC_coupled/phreeqc/ (last accessed on 15 July 2009).
- Peng G, van Elp J, Jang H, Que L Jr, Armstrong WH, Cramer SP (1995) L-Edge X-ray absorption and X-ray magnetic circular dichroism of oxygen-bridged iron complexes. *Journal of the American Chemical Society* **117**, 2515–2519.
- Peng X, Zhou H, Wu Z, Jiang L, Tang S, Yao H, Chen G (2007) Biomineralization of phototrophic microbes in silica-enriched hot springs in South China. *Chinese Science Bulletin* **52**, 367–379.
- Pecher K, McCubbery D, Kneeder E, Rothe J, Bargar J, Meigs G, Cox L, Nealon K, Tonner B (2003) Quantitative charge state analysis of manganese biominerals in aqueous suspension using scanning transmission x-ray microscopy (STXM). *Geochimica et Cosmochimica Acta* **67**, 1089–1098.
- Phoenix VR, Konhauser KO (2008) Benefits of bacterial biomineralization. *Geobiology* **6**, 303–308.
- Rajendran P, Muthukrishnan J, Gunasekaran P (2002) Current perspectives in nickel bioremediation strategies. *Indian Journal of Microbiology* **42**, 1–9.
- Richens DT (1997) *The Chemistry of Aqua Ions: Synthesis, Structure and Reactivity: A Tour Through the Periodic Table of the Elements*. John Wiley & Son Ltd, Chichester, UK, pp. 1–600.
- Riding R (2000) Microbial carbonates: the geological record of calcified bacterial-algal mats and biofilms. *Sedimentology* **47**, 179–214.
- Salt DE, Smith RD, Raskin I (1998) Phytoremediation. *Annual Review of Plant Physiology and Plant Molecular Biology* **49**, 643–668.
- Sar P, Kazy SK, Asthana RK, Singh SP (1999) Metal adsorption and desorption by lyophilized *Pseudomonas aeruginosa*. *International Biodeterioration & Biodegradation* **44**, 101–110.
- Saratovsky I, Wightman PG, Pastén PA, Gaillard J-F, Poepelmeier KR (2006) Manganese oxides: parallels between abiotic and biotic structures. *Journal of the American Chemical Society* **128**, 11188–11198.
- Scheidegger A, Borkovec M, Sticher H (1993) Coating of silica sand with goethite; preparation and analytical identification. *Geoderma* **58**, 43–65.
- Schultze-Lam S, Harauz G, Beveridge TJ (1992) Participation of a Cyanobacterial S layer in fine-grain mineral formation. *Journal of Bacteriology* **174**, 7971–7981.
- Schultze-Lam S, Ferris FG, Konhauser KO, Wiese RG (1995) In-situ silicification of an Icelandic hot spring microbial mat: implications

- for microfossil formation. *Canadian Journal of Earth Science* **32**, 2021–2026.
- Sette F, Sinkovic B, Ma YJ, Chen CT (1989) Crystal-field splitting of core excitations in ionic crystals. *Physical Review B* **39**, 11125–11130.
- Shiller AM, Stephens TH (2005) Microbial manganese oxidation in the Lower Mississippi River: methods and evidence. *Geomicrobiology Journal* **22**, 117–125.
- Stewart-Ornstein J, Hitchcock AP, Hernández-Cruz D, Henklein P, Overhage J, Hilpert K, Hale J, Hancock REW (2007) Using intrinsic X-ray absorption spectral differences to identify and map peptides and proteins. *Journal of Physical Chemistry B* **111**, 7691–7699.
- Tamura H, Furuichi R (1997) Adsorption affinity of divalent heavy metal ions for metal oxides evaluated by modeling with Frumkin isotherm. *Journal of Colloid and Interface Science* **195**, 241–249.
- Tani Y, Ohashi M, Miyata N, Seyama H, Iwahori K, Soma M (2004) Sorption of Co(II), Ni(II), and Zn(II) on biogenic manganese oxides produced by a Mn-oxidizing fungus, strain KR21-2. *Journal of Environmental Science and Health A* **39**, 2641–2660.
- Tazaki K (2000) Formation of banded iron-manganese structures by natural microbial communities. *Clays and Clay Minerals* **48**, 511–520.
- Tebo BM, Bargar JR, Clement BG, Dick GJ, Murray KJ, Parker D, Verity R, Webb SM (2004) Biogenic manganese oxides: properties and mechanisms of formation. *Annual Review Earth Planetary Science* **32**, 287–328.
- Templeton AS, Trainor TP, Traina SJ, Spormann AM, Brown GE Jr (2001) Pb(II) distributions at biofilm-metal oxide interfaces. *Proceedings of the National Academy of Sciences of the USA* **98**, 11897–11902.
- Templeton AS, Trainor TP, Spormann AM, Newville M, Sutton SR, Dohnalkova A, Gorby Y, Brown GE Jr (2003) Sorption versus biomineralization of Pb(II) within *Burkholderia cepacia* biofilms. *Environmental Science & Technology* **37**, 300–307.
- Theis TL, Singer PC (1974) Complexation of iron(II) by organic matter and its effect on iron(II) oxygenation. *Environmental Science and Technology* **8**, 569–573.
- Toner B, Fakra S, Villalobos M, Warwick T, Sposito G (2005) Spatially resolved characterization of biogenic manganese oxide production within a bacteria biofilm. *Applied and Environmental Microbiology* **71**, 1300–1310.
- Toner B, Manceau A, Webb SM, Sposito G (2006) Zinc sorption to biogenic hexagonal-birnessite particles within a hydrated bacterial biofilm. *Geochimica et Cosmochimica Acta* **70**, 27–43.
- Toporski JKW, Westall F, Thomas-Keppta KA, Steele A, McKay DS (2001) The simulated silicification of bacteria – new clues to the modes and timing of bacterial preservation and implications for the search for extraterrestrial microfossils. *Astrobiology* **2**, 1–25.
- Trcera N, Cabaret D, Rossano S, Farges F, Flank A-M, Lagarde P (2008) Experimental and theoretical study of the structural environment of magnesium in minerals and silicate glasses using X-ray absorption near-edge structure. *Physics and Chemistry of Minerals* **12**, 3.
- Urquhart SG, Turci CC, Tyliczszak T, Brook MA, Hitchcock AP (1997) Core excitation spectroscopy of phenyl- and methyl-substituted silanol, disiloxane, and disilane compounds: evidence for π -delocalization across the Si-C_{phenyl} bond. *Organometallics* **16**, 2080–2088.
- Urrutia MM, Beveridge TJ (1993) Mechanisms of silicate binding to bacteria cell wall *Bacillus subtilis*. *Journal of Bacteriology* **175**, 1936–1945.
- Urrutia MM, Beveridge TJ (1994) Formation of fine-grained metal and silicate precipitates on a bacterial surface (*Bacillus subtilis*). *Chemical Geology* **116**, 261–280.
- Urrutia M, Kemper M, Dotle R, Beveridge TJ (1992) The membrane-induced proton motive force influences the metal binding ability of *Bacillus subtilis* cell walls. *Applied Environmental Microbiology* **58**, 3837–3844.
- Villalobos M, Toner B, Bargar J, Sposito G (2003) Characterization of the manganese oxide produced by *Pseudomonas putida* strain MnB1. *Geochimica et Cosmochimica Acta* **67**, 2649–2662.
- Villalobos M, Bargar J, Sposito G (2005) Trace metal retention on biogenic manganese oxide nanoparticles. *Elements* **1**, 223–226.
- Villalobos M, Lanson B, Manceau A, Toner B, Sposito G (2006) Structural model for the biogenic Mn oxide produced by *Pseudomonas putida*. *American Mineralogist* **91**, 489–502.
- Warren LA, Ferris FG (1998) Continuum between sorption and precipitation of Fe(III) on microbial surfaces. *Environmental Science and Technology* **32**, 2331–2337.
- Warwick T, Ade H, Kilcoyne ALD, Kritscher M, Tyliczszak T, Fakra S, Hitchcock AP, Padmore HA (2002) A new bend magnet beam line for scanning transmission X-ray microscopy at the Advanced Light Source. *Journal of Synchrotron Radiation* **9**, 254–257.
- Warwick T, Andresen N, Comins J, Kaznacheyev K, Kortright JB, McKean JP, Padmore HA, Shuh DK, Stevens T, Tyliczszak T (2004) New implementation of an SX700 undulator beamline at the advanced light source. *AIP Conference Proceedings* **705**, 458–461.
- Weckesser J, Hofmann K, Jurgens UJ, Whitton BA, Raffelsberger B (1988) Isolation and chemical analysis of the sheaths. *Journal of General Microbiology* **134**, 629–634.
- Westall F, Boni L, Guerzoni E (1995) The experimental silicification of microorganisms. *Palaeontology* **38**, 495–528.
- Xu Y, Axe L (2005) synthesis and characterization of iron oxide-coated silica and its effect on metal sorption. *Journal of Colloid and Interface Science* **282**, 11–19.
- Xu Y, Axe L, Boonfueng T, Tyson TA, Trivedi P, Pandya K (2007) Ni(II) complexation to amorphous hydrous ferric oxide: an X-ray absorption spectroscopy study. *Journal of Colloid and Interface Science* **314**, 10–17.
- Yee N, Fein J (2001) Cd adsorption onto bacteria surfaces: a universal adsorption edge. *Geochimica et Cosmochimica Acta* **65**, 2037–2042.
- Yoon TH, Johnson SB, Benzerara K, Doyle CS, Tyliczszak T, Shuh DK, Brown GE Jr (2004) In situ characterization of aluminum-coating mineral-microorganism aqueous suspensions using scanning transmission x-ray microscopy. *Langmuir* **20**, 10361–10366.

SUPPORTING INFORMATION

Additional Supporting Information may be found in the online version of this article:

Fig. S1 Damage check images. (A) First detailed image of study area (<2 ms pixel⁻¹ total). (B) After first stack (0 1s, 70 images at 0.6 ms pixel⁻¹; ~45 ms total integrated). (C) After all February 2005 STXM 11 experiments: 0 1s stack, Fe stack (53 images at 0.45 ms pixel⁻¹), Mn stack (50 images at 0.3 ms pixel⁻¹) and Ni stack (35 images at 0.45 ms pixel⁻¹) ~120 ms total

integrated), (D) after C 1s stacks on STXM 532 in February 2005 (85 images at 0.8 ms ~200 ms total integrated), (E) after STXM 11 Si 1s stack in October 2005 [(F) after Si 1s stack (12 images at 0.8 ms ~210 ms total integrated), (F) after additional stacks at S 1s (65 images at 1 ms) and Al 1s edges (136 images at 2 ms)]. Although the dose changed a lot from edge to edge, all the data recorded required only ~500 ms pixel⁻¹ for total time, integrated over all measurements, a time where only the most radiation sensitive materials (such as PMMA) would show a significant damage.

Fig. S2 (A) Mg 1s spectrum of a Mg-rich region outside of the study area, compared with the spectra of cordierite and fosterite (Trcera *et al.*, 2008). The inset figure shows the Mg map of this area. (B) OD images at (i) 1303 and (ii) 1315.5 eV of the study area, along with (iii) their difference, and (iv) an overlay of the Mg signal (blue) and the 1303 eV image (gray scale). Aside from a few small particles, no Mg is detected.

Fig. S3 (A) OD image at 637.0 eV, before the onset of Mn 2p absorption. (B) OD image at 639.6 eV [peak of Mn(II) absorption]. (C) Difference.

Fig. S4 (A) Image at 639.6 eV. (B) Image at 642.4 eV taken from the Mn 2p stack, after the non-Mn signal had been subtracted. (C) Spectra extracted from the color regions showing strong differences in different regions of the sample.

Please note: Wiley-Blackwell are not responsible for the content or functionality of any supporting materials supplied by the authors. Any queries (other than missing material) should be directed to the corresponding author for the article.